Mon. Not. R. Astron. Soc. **337,** 1381–1406 (2002)

Deep spectroscopy of $z \sim 1$ 6C radio galaxies – I. The effects of radio power and size on the properties of the emission-line gas

K. J. Inskip,[1⋆] P. N. Best,[2] S. Rawlings,[3] M. S. Longair,[1] G. Cotter,[1] H. J. A. Röttgering[4] and S. Eales[5]

[1]*Cavendish Laboratory, Madingley Road, Cambridge CB3 0HE*
[2]*Institute for Astronomy, Royal Observatory Edinburgh, Blackford Hill, Edinburgh EH9 3HJ*
[3]*Department of Astrophysics, University of Oxford, Keble Road, Oxford OX1 3RH*
[4]*Sterrewacht Leiden, Postbus 9513, 2300 RA Leiden, the Netherlands*
[5]*Department of Physics and Astrophysics, University of Wales Cardiff, PO Box 913, Cardiff CF2 3YB*

Accepted 2002 August 22. Received 2002 August 22; in original form 2002 May 8

ABSTRACT

The results of deep long-slit optical spectroscopy for a sample of eight 6C radio galaxies at redshift $z \sim 1$ are presented. Emission-line ratios are derived for many emission lines with rest-frame wavelengths of 1500–4500 Å and the kinematic properties of the emission-line gas are derived from an analysis of the two-dimensional structure of the [O II] 3727-Å emission line at ≈5 Å spectral resolution.

In general, the 6C spectra display many characteristics similar to those of more powerful 3CR sources at the same redshifts. The emission-line region gas kinematics are more extreme for the smaller radio sources in the sample, which often display distorted velocity profiles. The ionization state of the emission-line region also varies with radio size: the spectra of large radio sources (>120 kpc) are consistent with photoionization by an obscured active galactic nucleus (AGN), whilst smaller (<120 kpc) sources typically exist in a lower ionization state and have spectra that are better explained by additional ionization due to shocks associated with the expanding radio source. The kinematic and ionization properties of the 6C radio galaxies are clearly linked. As for the 3CR sources, smaller radio sources also typically possess more extensive emission-line regions, with enhanced emission-line luminosities. A high-velocity emission-line gas component is observed in 6C 1019+39, similar to that seen in 3C 265.

It is clear that the best interpretation of the spectra of radio sources requires a combination of ionization mechanisms. A simple model is developed, combining AGN photoionization with photoionization from the luminous shock associated with the expanding radio source. The relative contributions of ionizing photons from shocks and the central AGN to an emission-line gas cloud vary with radio source size and the position of the cloud. This model provides a good explanation for both the ionization properties of the emission-line regions and the radio size evolution of the emission-line region extents and luminosities.

Key words: galaxies: active – galaxies: evolution – galaxies: ISM – radio continuum: galaxies.

1 INTRODUCTION

Extended emission-line regions are often observed around powerful radio galaxies. High-redshift ($z \gtrsim 0.5$) radio galaxies typically have more extensive emission-line regions than lower power radio sources at low redshift. These emission-line regions can be up to 100 kpc in size, and are often elongated and aligned along the radio jet axis (McCarthy 1993; McCarthy, Spinrad & van Breugel 1995). The kinematics of the emission-line gas of higher redshift radio galaxies are generally more extreme than those seen in low-redshift radio galaxies; more distant sources have larger emission-line full width at half-maximum (FWHM) and larger velocity shears. The luminosities of the emission lines are large, with rest-frame equivalent linewidths often exceeding 100 Å (e.g. Baum & McCarthy 2000).

Over the past few years it has become increasingly clear that, in addition to photoionization by an obscured active galactic nucleus (AGN), in some cases the emission-line gas may also be ionized by

⋆E-mail: kji@mrao.cam.ac.uk

radiative shocks associated with the radio source. Evidence for this includes the fact that, whilst the spectra of low-redshift sources are well explained by AGN photoionization, the emission-line regions of more distant galaxies do not always display the characteristic line ratios of photoionized regions, and require alternative heating mechanisms. Furthermore, observations of individual sources reveal features suggesting significant interactions of the radio jet with the interstellar medium (ISM) of the host galaxy. Shocks associated with the passage of the radio source clearly influence the kinematics and morphology of the emission-line gas, and can also affect the ionization state within the gas. Another potential source of ionizing photons is ultraviolet (UV) emission from a young stellar population. Dey et al. (1997) find that the extended UV continuum emission from 4C 41.17 ($z = 3.8$) is unpolarized, suggesting that scattered light from the AGN is not a dominant source of UV photons. This galaxy appears to have undergone a major epoch of star formation at $z \sim 4$. At lower redshifts, the stellar populations of radio galaxies are generally old. Most 3CR radio galaxies at $z \sim 1$ exhibit strong continuum polarization ($\sim$10 per cent, e.g. di Serego Alighieri, Cimatti & Fosbury 1994); scattered light from an obscured AGN provides a large proportion of the extended UV continuum. Although small amounts of radio source jet-induced star formation are possible, this is clearly not the dominant source of aligned continuum emission, nor can it be a major source of ionizing photons for objects at $z \sim 1$.

Spectroscopic observations of a sample of 14 3CR radio galaxies at $z \sim 1$ by Best, Röttgering & Longair (2000a,b) showed that the ionization state of such sources is strongly correlated with radio size, smaller radio sources generally existing in a lower ionization state. In addition, radio sources with linear sizes $\lesssim$150 kpc typically have greater emission-line fluxes and broader linewidths than their larger counterparts. The emission-line ratios of smaller sources are in good agreement with the predictions of shock ionization models, and their observed kinematics are more disturbed. The irregularities in the velocity structures of the small sources are likely to be due to shock acceleration of the emission-line gas clouds. Compression of the emission-line gas clouds by the shock front and the ionizing photons associated with it combine to lower the ionization state of the gas in smaller sources. The properties of the larger, older, radio sources, for which the shocks associated with the expansion of the radio cocoon are long in the past, are well explained by photoionization models.

A spectroscopic study of four intermediate-redshift 3CR galaxies by Solórzano-Iñarrea, Tadhunter & Axon (2001) found evidence for shock acceleration of the emission-line gas in the extended emission-line regions (EELRs) of all four galaxies. The disturbed kinematics of these sources are reflected in the emission-line spectra by line splitting and/or underlying broad components. Two of these sources have radio sizes comparable to the physical extent of the emission-line region, and both show evidence for an underlying broad component in their emission lines. Of the two sources with radio sizes significantly larger than their emission-line regions, only one shows evidence for an underlying broad component, although both sources exhibit line splitting. Both of these features can be related to the effects of shocks on the emission-line gas.

It is clear that the age of a radio source and the dominant ionization mechanism play a determining role in the observed properties of the emission-line regions of powerful high-redshift radio galaxies. It is important to understand exactly how radio luminosity correlates with the EELR properties; the precise effects of radio jet power on shock acceleration and the ionization mechanism are still uncertain. To this end, we have carried out deep spectroscopic observations of a complete sample of eight 6C radio galaxies at $z \sim 1$. In this paper we investigate the effects of radio power on the ionization and kinematic properties of emission-line regions by contrasting the properties of our sample of 6C galaxies with those of the more powerful 3CR galaxies at similar redshifts. A comparison with a sample of low-redshift 3CR sources matched in radio power to the 6C subsample will also enable us to break the degeneracy between redshift and radio power present in any flux-limited sample; this analysis is deferred to a second paper. Overall, this research is aimed at adding to our understanding of: (i) the physics of the ISM in relatively extreme conditions, (ii) the impact of AGN activity on its nearby environment, and (iii) the origin of the cool gas that forms the extended emission-line regions.

The layout of the paper is as follows. Section 2 gives details of the sample selection, the observations, and the data reduction techniques. In Section 3, the results of the spectroscopic observations are presented, including a 2D analysis of the [O II] 3727-Å emission line. Section 4 describes an analysis of the ionization and kinematical properties of the emission-line gas and compares these with the results of the more powerful 3CR galaxies at the same redshift. Our results are discussed in Section 5, and a summary of our conclusions is given in Section 6.

Throughout the paper, values for the cosmological parameters of $\Omega_0 = 0.3$, $\Omega_\Lambda = 0.7$ and $H_0 = 65$ km s^{-1} Mpc^{-1} are assumed.

2 OBSERVATIONS

2.1 Sample selection and observational procedures

The observed radio galaxies were selected from the 6CER sample[1] (Rawlings, Eales & Lacy 2001), a revised version of the sample originally defined by Eales (1985). This revised sample is complete, and consists of 59 radio sources with flux densities in the range $2.0\,\mathrm{Jy} < S_{151} < 3.93\,\mathrm{Jy}$ at 151 MHz which lie in the region of sky $08^{\mathrm{h}}20^{\mathrm{m}} < \mathrm{RA} < 13^{\mathrm{h}}01^{\mathrm{m}}$ and $34^\circ < \delta < 40^\circ$. Radio, optical and infrared studies have been carried out for a complete subsample of 11 radio galaxies, selected from this sample within the redshift range $0.85 < z < 1.5$ (Best et al. 1999; Inskip et al., in preparation). The spectroscopic study of these galaxies was restricted to eight objects with $z < 1.2$, in order to include only those galaxies for which the observed wavelength of the 4340-Å Hδ line would be observed at wavelengths $\lambda \lesssim 9100$ Å, and thus potentially observable. The three excluded galaxies all have redshifts $z > 1.37$. This subsample of 6C galaxies is well matched to the nearly complete subsample of 14 3CR galaxies studied by Best et al. (2000a), which lies within the same redshift range.

The observations were carried out on 1999 March 20–22 and 2000 February 28–March 02, using the dual-beam ISIS spectrograph (Carter et al. 1994) on the William Herschel Telescope (WHT). To enable the highest throughput at short wavelengths, the 5400-Å dichroic was used. In the blue arm, the R158B grating was used in conjunction with the EEV12 charge-coupled device (CCD). This low-dispersion grating provided a spatial scale of 0.4 arcsec pixel^{-1}, a spectral scale of 2.7 Å pixel^{-1}, a spectral resolution of approximately 19 Å and a wide spectral coverage from 3000 Å to the dichroic at about 5400 Å. With this arrangement, we were able to measure accurately the strengths of emission lines at short wavelengths. In the red arm of the spectrograph, the R316R grating was used in conjunction with the TEK4 CCD. This provided a spatial

[1] Up-to-date information for the revised 6CE sample can be found at: http://www-astro.physics.ox.ac.uk/~sr/6ce.html

scale of 0.36 arcsec pixel^{-1}, a spectral scale of 1.49 Å pixel^{-1} and spectral resolution of approximately 5 Å. The observed wavelength coverage in a single grating position is 1500 Å. Two different central wavelengths were generally used; the first value selected gave a rest-frame wavelength coverage from [Ne V] 3426 Å out to approximately 4000 Å, and the second typically covered the spectrum from 3600 Å to Hγ, or Hδ for the higher redshift sources. The spectral range provided by each selected central wavelength was chosen to include the 3727-Å [O II] line, and also to enable measurement of either the [Ne III] 3869 Å/[Ne V] 3426-Å line ratio or the Balmer line fluxes of the source in question. Full details of the observations are given in Table 1.

2.2 Observations and data reduction

Long-slit spectra were obtained for all eight galaxies, with total integration times varying between 2 and 5.5 h, averaging 3.5 h in each arm. Red arm exposures were typically split into individual exposures of 1500 s in length to aid the removal of cosmic rays. Individual blue arm exposures were taken for twice as long in order to reduce the fractional read noise contribution. These exposures were sky background limited, as a result of the binning of the blue arm CCD and the longer exposure times. In most cases, the slit was oriented along the radio axis of the source. For 6C 1256+36, exposures at several different sky position angles (PAs) were taken, in order to include other objects in the field suspected of being cluster members around the radio galaxy (to be discussed elsewhere). Two different PAs were used for 6C 1011+36 in order to position the slit along the axes of both the radio jets and the extended optical emission. Details of the observations are included in full in Table 1.

The seeing varied from 0.7 to 2.0 arcsec during the 1999 March observations. For the 2000 observations, the seeing was more changeable. The seeing on the first night was between 2 and 2.6 arcsec, but decreased to ≈1.8 arcsec throughout the second night. The seeing on the final night increased steadily from 1.9 arcsec up to non-photometric conditions of greater than 3 arcsec seeing, at which point further observations became unusable.

Standard packages within the NOAO IRAF reduction software were used to reduce the raw data. Corrections were made for overscan bias subtraction, and the data were then flat-fielded using internal calibration lamp observations. The flat-field images were made using the same instrumental setup as the observations for each source, in order to minimize fringing effects. As red arm images of the galaxies were taken at one or more different observed wavelength ranges for each object, several flat fields had to be taken for each galaxy, and the flat-field exposures were interspersed between the observations on-source. Taking care not to subtract any of the extended line emission, the sky background was removed.

Table 1. Details of the ISIS observations. Where more than one slit position angle (PA) is listed on a single line, the radio galaxy emission-line data were combined in two dimensions, owing to the similarity of the 2D emission-line spectra.

Source	Redshift	Observation date (dd/mm/yy)	Slit width (arcsec)	Isis arm	Exposure time (s)	Wavelength range (Å)	Slit PA (deg)
6C 0943+39	1.035	21/03/99, 22/03/99	1.5	blue	15360[a]	3100–5400	105[b]
		21/03/99, 22/03/99, 01/03/00	1.5–2.5	red	19950	6900–9000	105, 110[b]
6C 1011+36	1.042	21/03/99	1.5	blue	3000	3100–6000[c]	47[b]
		21/03/99	1.5	red	3000	6900–8250	47[b]
		21/03/99, 01/03/00	1.5–2.5	blue	9320	3100–6000	345[d]
		21/03/99[e]	1.5–2.5	red	9000	6900–9000	345[d]
6C 1017+37	1.053	22/03/99, 29/02/00	1.5–2.5	blue	15440	3100–5400	48[b]
		22/03/99, 29/02/00	1.5–2.5	red	13180	6900–9000	48[b]
6C 1019+39	0.922	28/02/00	1.5–2.0	blue	9360[a]	3100–5400	61[b]
		28/02/00, 01/03/00	1.5–2.5	red	14800	6400–7900[f]	61[b]
6C 1129+37	1.060	21/03/99, 22/03/99	1.5	blue	12590	3100–5400	105[b]
		21/03/99, 22/03/99	1.5	red	12000	6950–8450[g]	105[b]
6C 1217+36	1.088	29/02/00	2.0	blue	10540	3500–5400	61[b]
		29/02/00	2.0	red	7300[h]	7100–8600	61[b]
6C 1256+36	1.128	21/03/99, 22/03/99	1.5–2.0	blue	9390	3100–5400	40[b], 22[i], 0[i]
		21/03/99, 22/03/99	1.5–2.0	red	9000	7000–9000	40[b], 22[i], 0[i]
		21/03/99, 22/03/99	1.5–2.0	blue	6240	3100–5400	115[i], 79[i]
		21/03/99, 22/03/99	1.5–2.0	red	6000	7250–9000	115[i], 79[i]
6C 1257+36	1.004	28/02/00	2.0–2.5	blue	11720	3100–5400	317[b]
		28/02/00	2.0–2.5	red	11220	6750–8250[g]	317[b]

[a] The seeing conditions on 01/03/00 were extremely poor. Some blue arm observations on this night were necessarily excluded because of their very low signal-to-noise ratio.
[b] Slit aligned along the radio axis.
[c] Blue arm data beyond the dichroic are included because of the high signal-to-noise ratio of the Mg II 2800-Å line.
[d] Slit aligned with the optical emission.
[e] The red arm observations of 6C 1011+36 on 01/03/00 were excluded because of the very poor seeing conditions.
[f] The [Ne V] 3426-Å line for 6C 1019+39 is very weak, and only one red arm central wavelength was used in order to maximize the signal-to-noise ratio of this emission line.
[g] Only one red arm central wavelength was used for this object, because of the loss of the latter half of the night of 01/03/00.
[h] The red arm exposure time for 6C 1217+36 is considerably lower than that for the blue arm, as a result of technical problems during the observations.
[i] Slit angled in other directions to include other objects in the field.

All observations of a galaxy taken using the same central wavelength and slit PA were combined as 2D spectra. For both 6C 0943+39 and 6C 1011+36, the slit PAs of different observations differ by 5°. With such a small difference in PA, essentially the same regions of the galaxies are sampled by the observations, and so the 2D spectra of each of these sources were combined at this stage. For 6C 1256+36, five different slit PAs were used. Examination of the 2D structure of the emission lines showed no apparent variation for observations with slit PAs within ∼40° of each other. The 2D spectra of this source have therefore been combined in two groups, with slit PAs of 0°, 22° and 40°, and 79° and 115°, respectively. As the emission-line region of this source is <3 arcsec in extent, the observations combined at this stage essentially sample the same region of the galaxy. Sources for which observations had been made at several different central wavelengths, or very different slit PAs in the case of 6C 1256+36, could not be fully combined at this stage. 1D spectra were extracted from the central 4 arcsec of the combined (or partially combined) data, and wavelength-calibrated using observations of the internal CuNe and CuAr arc lamps, which removed the large-scale non-linearities. A slight linear shift of wavelength was sometimes also required, and was determined from unblended sky lines (Osterbrock & Martel 1992). The 1D spectra of sources taken with more than one central wavelength and/or several slit PAs were fully combined at this point. Observations of the spectrophotometric standard stars G191b2b, HZ44, G99−37 and BD+26 26, observed in the same instrumental setup as the observations of the galaxies, were used to provide accurate flux calibration of the final 1D spectra. A comparison of our spectra with the line luminosities of Rawlings et al. (2001) suggests that use of narrower slits coupled with occasional poor seeing may have led to some slit losses, particularly for the sources with more extensive emission-line regions. To create 2D spectra of the [O II] line for the analysis of the kinematic properties of the emission-line gas, observations of a particular galaxy were combined where these were taken at sufficiently close slit PAs, and the appearance of the [O II] emission lines were indistinguishable.

3 RESULTS

3.1 Fitting the spectroscopic data

The 1D spectra for both the red and blue arms are displayed in panels (a) and (b) of Figs 1, 2, 4–8 and 10. The fluxes of various emission lines relative to [O II] 3727 Å are tabulated in Table 2, as well as their equivalent widths and the mean continuum flux density in various regions of the spectrum. The flux ratios and flux densities tabulated in Table 2 have been corrected for Galactic extinction, using values for the H I column density of the Milky Way taken from the NASA Extragalactic Database (NED), and the parametrized Galactic extinction law of Howarth (1983). The redshifts obtained from the spectra of the eight sources agree with those of Rawlings et al. (2001), confirming less-certain single-line redshifts in four cases.

A 2D region around the [O II] 3727-Å emission line was extracted in order to study the velocity structure of the gas [Figs 1(c), 2(c), 3(a), 4–8(c), 9(a) and 10(c)]. From these, a sequence of 1D spectra were extracted along the slit direction, stepped every 0.72 arcsec (two pixels), with widths of 1.44 arcsec (four pixels). The extracted spectra were then analysed following the procedure described in Best et al. (2000a), which is summarized below.

After allowing for continuum subtraction, the data were fitted by successive Gaussian components, which were only accepted if the signal-to-noise ratio (S/N) was greater than 5 and the FWHM larger than the instrumental resolution. The combination of Gaussians providing the best fit (that with the lowest reduced χ^2) to the extracted spectra determined the maximum number of velocity components that could realistically be fitted to the data.

This approach allows us to search for high-velocity components in the emission-line gas, or other structures incompatible with a fit to a single velocity component. The integrated emission-line flux, the velocity relative to that at the centre of the Galaxy, and the emission-line FWHM were determined for each Gaussian fit. In order to calculate the emission-line FWHM, it was necessary to deconvolve it by subtracting in quadrature the instrumental FWHM, as determined from unblended sky lines. This procedure assumes that the line emission illuminates the slit in a similar manner to the background sky emission, which is an adequate approximation for narrow slits and imperfect seeing conditions. Errors were also calculated for these three parameters.

This method is optimized for determining the variation of the kinematic properties of the galaxies with position very accurately. However, the flux levels in each extracted 1D spectrum as a percentage of the total [O II] emission-line flux of the galaxy are fairly low. This, and the low S/N levels in the spectroscopic data, makes identification of any broad emission-line structures, such as those found by Solórzano-Iñarrea et al. (2001), much more difficult. A single Gaussian fit was not always ideal for our data, with the profiles of some sources exhibiting weak wings on either the red or blue side of the line. These may simply indicate that the intrinsic line-shape is non-Gaussian or possibly could be associated with a weaker emission component at a different velocity which was too faint to be individually identified, or a faint broad-line component. By extracting a lower spatial resolution spectrum (typically seven to nine pixels instead of four) from the 2D [O II] line data, the emission-line flux is increased, improving the likelihood of identifying an underlying broad component. However, by extracting the data over a larger spatial extent of the emission-line region, any variations in the kinematics with position introduce ambiguities into the extracted 1D spectrum. A search for broad components in the emission lines of the 6C galaxies and the 3CR sample of Best et al. (2000a) was carried out, but gave inconclusive results (see Appendix A).

The results of fitting narrow lines to the 2D [O II] emission line are illustrated in panels (d)–(f) of Figs 1, 2, 4–8 and 10, and by panels (b)–(d) of Figs 3 and 9, as detailed in the figure captions. Noteworthy features for all objects are outlined below.

6C 0943+39 (Fig. 1) has the most irregular 2D [O II] 3727-Å emission-line profile of all eight 6C galaxies studied. The emission-line region is fairly large with a spatial extent of ∼70 kpc, and the FWHM varies greatly with position, as can be seen from its asymmetric shape. The FWHM of the [O II] line at 860 km s^{-1} is greater than average for the sample. 6C 0943+39 has a high [O II] luminosity and the strengths of some of the other emission lines from this source are amongst the strongest in the sample, although the Balmer lines in the spectra are so weak that they cannot be detected to the 3σ limit of 2.65×10^{-20} W m^{-2} (assuming a velocity width of 300 km s^{-1}).

6C 1011+36 was observed at two different sky PAs: with the slit aligned along the radio axis (Fig. 2) and at ≈60° to this, along the axis of the extended optical emission (Fig. 3). The 2D structure of the [O II] line appears similar in both orientations of the slit, and is particularly compact. 6C 1011+36 has the joint smallest physical size for the emission-line region, and the lowest maximum FWHM at 400 km s^{-1}. Its profile is very smooth, and probably consistent

Table 2. Spectroscopic properties of the 6C radio galaxies. See 'Notes on Table 2' that follow.

Source		6C 0943	6C 1011	6C 1017	6C 1019	6C 1129	6C 1217	6C 1256	6C 1257
Redshift		1.035	1.042	1.053	0.922	1.060	1.088	1.128	1.004
Radio size (kpc)		92	444	65	67	141	38	155	336
Milky Way $E(B-V)$		0.018	0.013	0.008	0.013	0.030	0.017	0.014	0.014
Integrated [O II] 3727-Å flux		5.01	1.24	6.86	2.43	5.14	0.51	2.09	2.24
C IV 1549 Å	Flux ratio	38.0	543	123	*	29.3	*	45.0	*
	Error	9.8	111	24.9	*	7.6	*	22.6	*
	Equiv. width	103	90	151	*	–	*	–	*
He II 1640 Å	Flux ratio	36.8	197	59.0	*	16.7	*	34.5	*
	Error	8.9	42.8	12.4	*	4.9	*	17.3	*
	Equiv. width	97	34	66	*	39	*	–	*
C III] 1909 Å	Flux ratio	29.6	161	57.9	58.8	22.4	42.4	18.7	69.6
	Error	6.1	32.7	11.9	22.7	4.8	18.2	9.4	22.2
	Equiv. width	49	43	58	43	58	22	–	25
C II] 2326 Å	Flux ratio	15.7	33.9	20.4	22.2	1.9	35.1	9.1	12.1
	Error	3.4	7.3	4.1	4.6	1.5	25.6	4.6	5.0
	Equiv. width	23	9	24	65	–	18	–	14
[Ne IV] 2425 Å	Flux ratio	10.9	87.9	23.6	4.5	16.0	7.8	4.3	23.2
	Error	2.4	17.4	4.7	2.9	4.6	7.4	2.2	7.1
	Equiv. width	17	26	28	14	58	–	–	27
Mg II 2798 Å	Flux ratio	*	185	*	–	*	*	*	*
	Error	*	50.5	*	–	*	*	*	*
	Equiv. width	*	76	*	–	*	*	*	*
[Ne V] 3426 Å	Flux ratio	16.1	83.1	25.4	2.1	11.6	5.8	14.8	28.6
	Error	4.7	17.6	5.1	1.9	3.0	4.6	5.8	6.4
	Equiv. width	36	38	45	–	52	3	26	33
[O II] 3727 Å	Flux ratio	100	100	100	100	100	100	100	100
	Equiv. width	216	41	195	58	226	59	147	83
[Ne III] 3869 Å	Flux ratio	35.5	98.4	32.5	17.3	30.0	5.8	17.7	22.8
	Error	8.3	20.7	6.6	4.7	6.0	5.4	4.9	4.9
	Equiv. width	94	39	69	11	56	4	34	25
Hζ 3889 Å	Flux ratio	–	21.0	7.3	–	–	–	12.4	8.5
	Error	–	6.7	1.5	–	–	–	3.7	2.8
	Equiv. width	–	8	16	–	–	–	24	10
Hϵ + [Ne III] 3967 Å	Flux ratio	5.9	33.9	12.5	–	9.7	13.7	–	13.4
	Error	2.7	9.5	2.5	–	2.5	6.4	–	13.4
	Equiv. width	9	13	29	–	17	6	–	12
Hδ 4102 Å	Flux ratio	–	10.5	19.0	–	–	–	–	–
	Error	–	9.1	4.0	–	–	–	–	–
	Equiv. width	–	–	53	–	–	–	–	–
Hγ 4340 Å	Flux ratio	–	49.2	16.3	*	*	*	*	*
	Error	–	14.3	3.2	*	*	*	*	*
	Equiv. width	–	11	47	*	*	*	*	*
Mean flux density	2100–2300 Å	1.45	2.41	2.60	0.93	0.72	1.92	0.01	1.73
Error		0.21	0.30	0.32	0.32	0.13	0.47	0.04	0.49
Mean flux density	2450–2700 Å	1.17	–	–	0.96	–	–	–	1.01
Error		0.23	–	–	0.32	–	–	–	0.37
Mean flux density	3500–3700 Å	1.01	1.22	1.63	2.63	0.74	1.01	0.52	1.67
Error		0.16	0.20	0.23	0.33	0.15	0.27	0.12	0.25
Mean flux density	4050–4250 Å	1.09	2.11	0.68	–	–	–	0.87	1.91[a]
Error		0.31	0.57	0.46	–	–	–	0.39	0.53[a]

[a] Shorter wavelength range has been used in measuring the flux density.

Notes on Table 2: The [O II] 3727-Å integrated flux (units of 10^{-19} W m^{-2}) corresponds to the line flux along the entire length of the slit calculated by integrating the [O II] 3727-Å intensities shown in Figs 1–10(d). All the flux ratios and flux densities quoted in this table are corrected for Galactic extinction using the $E(B-V)$ for the Milky Way from the NASA Extragalactic Database (NED) and the parametrized Galactic extinction law of Howarth (1983). All flux ratios are measured relative to [O II] 3727 Å (value of 100) within the extracted 1D spectrum. The error on the [O II] 3727-Å line flux is dominated by calibration errors, estimated to be $\lesssim$10 per cent. Errors on the other lines and this calibration error are added in quadrature with the errors arising from photon statistics. There may be a small $\lesssim$5–10 per cent systematic offset between the red and blue arm measurements due to different spatial extraction regions – the extracted regions are of the same spatial extent, but may not be centred on the same position. Galaxies may not always be completely centred in the slit at the red and blue extremes as a result of differential refraction, as the slit position angle was not necessarily aligned with the parallactic angle. This should be minimal, however, as observations were generally taken at as low an airmass as possible, with a maximum value typically $<$1.3. Equivalent widths are measured in the rest frame of the galaxy. A dash is used to represent emission lines of such low flux as to be unobservable, and asterisks are used to represent emission lines outside the wavelength range covered by our spectra. Mean continuum flux densities for line-free wavelength ranges (or as much of the range as possible provided at least 100 Å are covered in the spectrum) are measured from the extracted 1D spectrum; the (weak) Hδ emission line was subtracted from the spectrum before calculating the mean continuum level for the wavelength range 4050–4250 Å. Values are in units of 10^{-21} W m^{-2} Å^{-1}; the uncertainty given is the error on the mean value in that wavelength region.

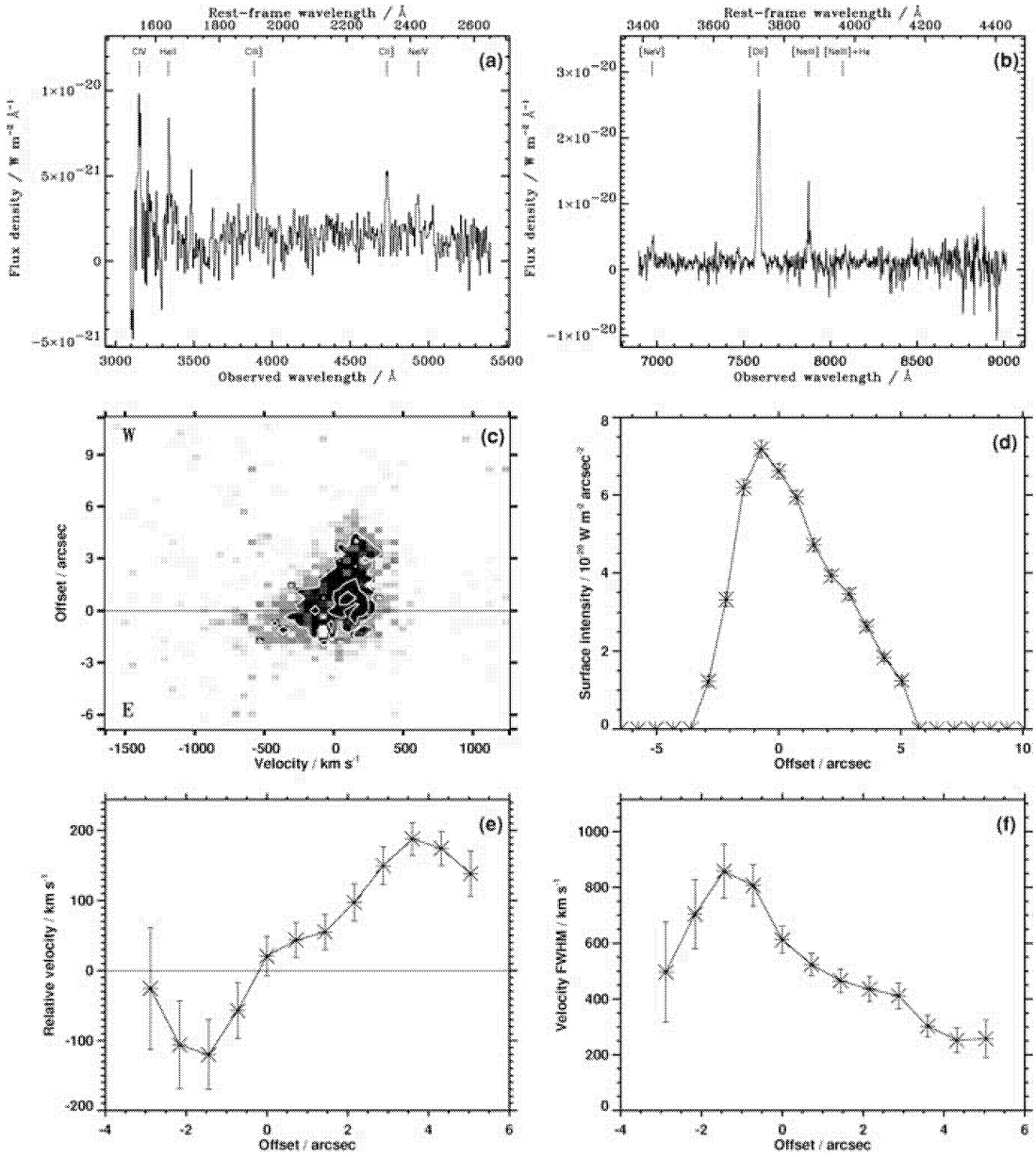

Figure 1. Spectroscopic data for 6C 0943+39. (a) 1D spectrum extracted from the blue arm. (b) 1D spectrum extracted from the red arm. Emission lines are labelled in both panels. (c) 2D extracted image of the [O II] 3727-Å emission line. Offset is measured in both 'positive' and 'negative' sky directions from the continuum centroid as defined by the labelling in the left-hand corners of this panel. Contour levels are for 100, 75 and 50 per cent of the maximum surface brightness level. (d) Surface brightness of the [O II] 3727-Å emission as a function of position along the slit. (e) Relative velocity of the fitted Gaussian peak as a function of slit position. (f) The variation of the fitted Gaussian profile FWHM as a function of slit position.

with rotation. One interesting point is that the Balmer lines of this source are relatively luminous, although it has the second lowest integrated [O II] flux of the sample.

6C 1017+37 (Fig. 4) is one of the smaller radio sources and possesses a strong [O II] 3727-Å emission line. Its profile is relatively smooth, a feature more characteristic of larger radio sources (Best et al. 2000a,b). The maximum FWHM and velocity range are similar to those of other small sources, but its emission-line ratios are closer to those of the larger ones. This apparent dichotomy will be discussed in more detail later.

6C 1019+39 (Fig. 5) has fairly weak carbon emission lines compared to other galaxies in this sample, but has perhaps the most prominent 4000-Å break, although the strength of this break may be influenced by the presence of the 7600-Å sky absorption feature, for which no correction has been made. Balmer lines are not identified to a 3σ flux density limit of 3.5×10^{-20} W m^{-2} (assuming a velocity width of 300 km s^{-1}). The 2D structure of the [O II] 3727-Å emission line is also unique in the irregularity of its structure. It appears that 6C 1019+39 is fairly likely to possess more than one velocity component in the emission-line gas, including a high-velocity component at 700 km s^{-1} which seems to be spatially close to the centre of the galaxy and appears to have a fairly narrow FWHM. This high-velocity component is similar to others observed at high and low redshifts, e.g. 3C 265 and 3C 405 respectively (Tadhunter 1991). Such high-velocity components may provide

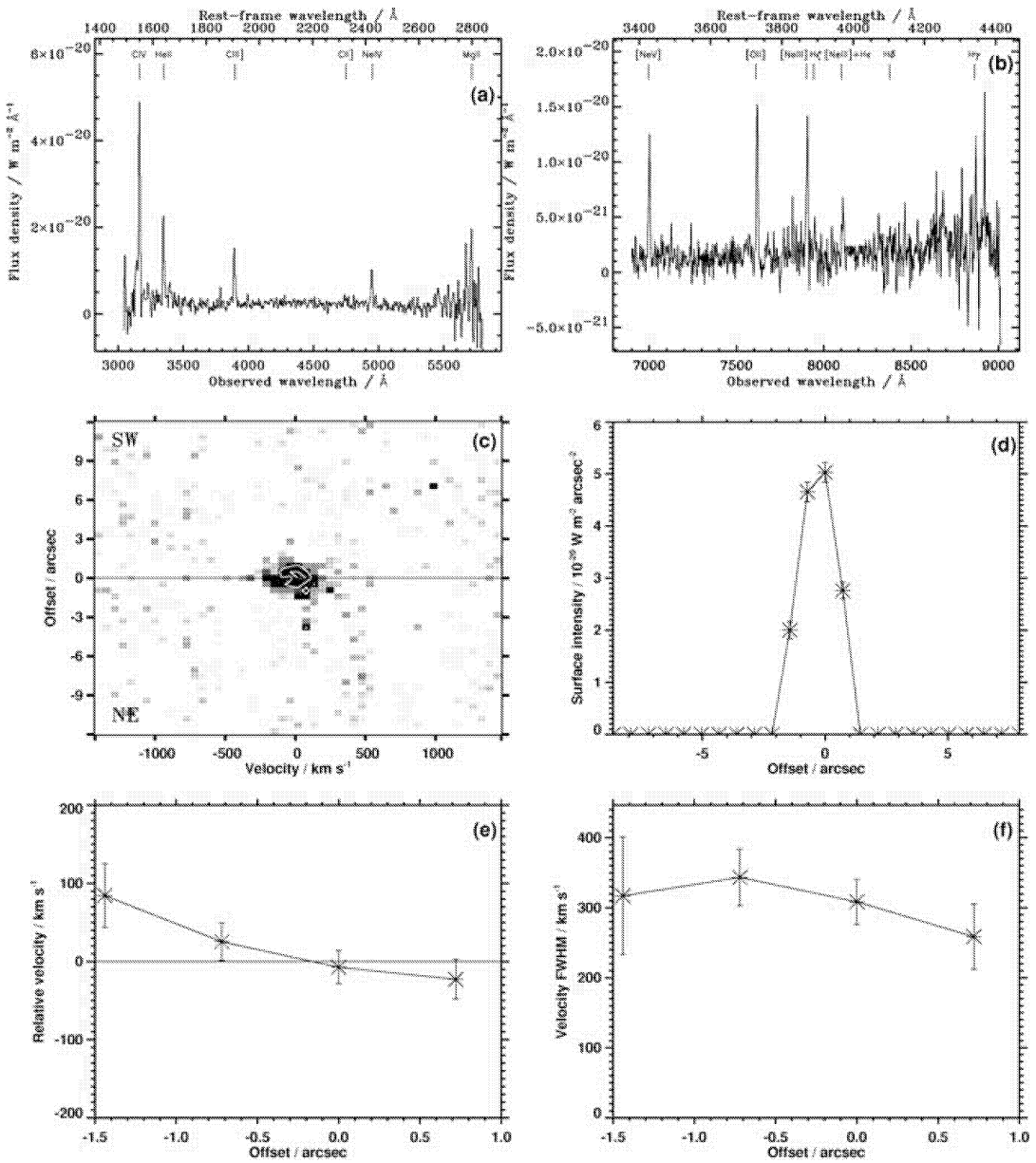

Figure 2. Spectroscopic data for 6C 1011+36 with the slit aligned along the radio axis at an angle of 47°. Contour levels in (c) are at 75 and 100 per cent of the maximum surface brightness level. Offset directions are as labelled in (c). Other details as in Fig. 1.

direct evidence for shock acceleration of the emission-line gas due to interactions with the radio jet (Solórzano-Iñarrea et al. 2001).

6C 1129+37 (Fig. 6) does not exhibit any observable Balmer lines, but other emission lines appear reasonably prominently in these spectra. Optical and infrared imaging of this source (Inskip et al., in preparation) shows a fair amount of diffuse aligned emission, and two elliptical galaxies, perhaps interacting. The east galaxy is roughly 0.1 mag brighter in the K band than that to the west, and, whilst the radio data show no central core (Best et al. 1999), we tentatively identify the radio source with the eastern galaxy of the two, which appears to lie more directly between the two lobes of radio emission than does the western galaxy. The 2D image of the [O II] line has been centred (offset = 0 on Fig. 6) on the east galaxy; the position of the eastern galaxy is identified by the solid line, and is coincident with the peak in the [O II] emission. The position of the western galaxy is identified by the dotted line. Further detailed discussion of this source is given in the paper presenting the imaging data. The velocity profile of the [O II] line for this source appears flat near the companion galaxy. The mean velocity of the extended emission-line region gas surrounding the radio galaxy varies smoothly with spatial position and is consistent with either rotation or outflow.

6C 1217+36 (Fig. 7) is considerably different from the rest of the sample. Not only is it the smallest radio source, but it also apparently does not possess a Fanaroff–Riley type II (FRII) radio structure (Best et al. 1999). The continuum level is slightly greater than the average for the sample, but the emission lines are very much fainter than those of any other object. Infrared and optical imaging of this source (Inskip et al., in preparation) show a passive giant elliptical galaxy, its magnitude following the K–z relation (infrared

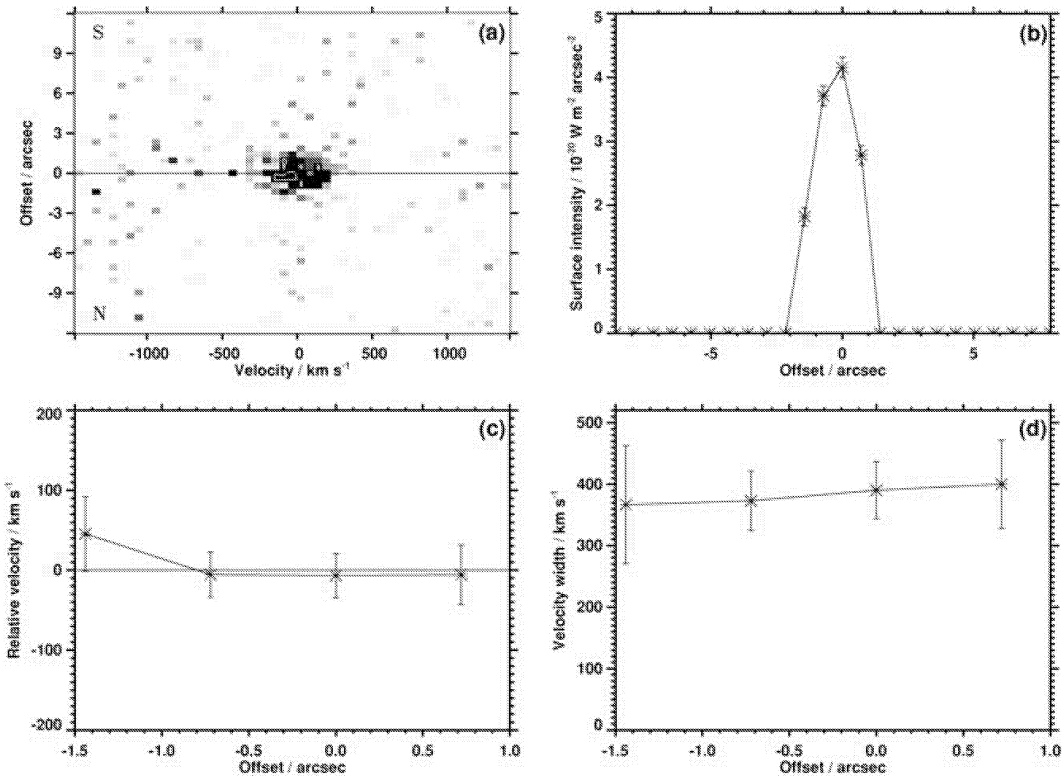

Figure 3. Spectroscopic data for 6C 1011+36, at a sky PA of 345° (aligned with the optical emission, at ∼60° to the radio axis). Parts (a)–(d) match captions (c)–(f) in Fig. 1. Offset directions are as labelled in (a). Contour levels in (a) are at 90 per cent of the maximum surface brightness level.

Hubble diagram) for these sources. The emission lines observed for this source are more believable in the 2D spectra – as shown for [O II] in Fig. 7(c) – than can be displayed here in one dimension, but are still very faint relative to the continuum emission. However, the redshift obtained is in agreement with that given by Rawlings et al. (2001). Identifications have been made for most of the oxygen, carbon and neon emission lines expected in the spectra. The 2D structure of the [O II] line does not appear particularly large in spatial extent, and is in fact the smallest in the sample. However, this may be due to the poor S/N in the spectra of this object. The maximum FWHM of this emission line is also the smallest of the sample, but the very low flux of this line may perhaps have led to an underestimate of this value when compared with the FWHM of the remainder of the sample. Owing to the high noise levels and the fact that this source is atypical of the $z \sim 1$ 6C subsample in many ways (including its anomalous non-FRII radio structure), this source has been excluded from any statistical analysis of the larger sample.

6C 1256+36 (Figs 8–9) was observed at five different sky PAs: along the radio axis (40°), and also at angles of 0°, 22°, 79° and 115°. This was carried out in order to obtain spectra for other objects in the field. An investigation of a possible $z \sim 1$ cluster will be presented elsewhere. The [O II] line of this source is small in spatial extent, and the velocity profile displays little variation with slit orientation. The redshift of this source was found to be 1.128 from our spectra; a previously published value of 1.07 (Eales et al. 1997) was an inaccurate estimate from an at-the-telescope reduction of the Rawlings et al. (2001) spectra.

6C 1257+36 (Fig. 10) is the second largest radio source of the sample, but the spatial extent of the [O II] 3727-Å line is also fairly large at about 60 kpc. Unfortunately, the [O II] line of this source is coincident with a bright sky line, leading to the low S/N in the 2D emission line. Despite this, the relative velocity and FWHM vary fairly smoothly with spatial position. The size of the emission-line region is the second largest in the subsample and, from the results of Best et al. (2000b) for 3CR galaxies, this is unexpected for such a large radio source. However, an examination of the radio data for this source (Best et al. 1999) shows a jet knot very close to the host galaxy, also associated with a blue feature in the *HST* images (Inskip et al., in preparation). The jet shocks associated with the production of this hotspot may induce many small radio source features into the ionization and kinematic properties of this galaxy.

4 COMPARISON WITH A MATCHED SAMPLE OF 3CR GALAXIES

4.1 Composite spectra

Red and blue arm composite spectra have been created for the $z \sim 1$ 6C subsample, excluding 6C 1217+36 because of its very low signal-to-noise ratio. The spectra were combined in the same rest frame, scaled according to their continuum flux and weighted by the continuum S/N. The 6C combined spectra are displayed in Fig. 11, and line ratios relative to [O II] 3727 Å are listed in the fourth data column in Table 3. As the flux density scale of the resulting red and blue arm composite spectra is arbitrary, the line ratios in the blue arm relative to [O II] 3727 Å need calibration. This was done by calculating the C III] 1909 Å/[O II] 3727-Å ratio, using the mean C III]/[O II] ratio for the entire 6C $z \sim 1$ subsample.

The 3CR subsample of Best et al. (2000a,b) displays considerable spectral variations between photoionized radio

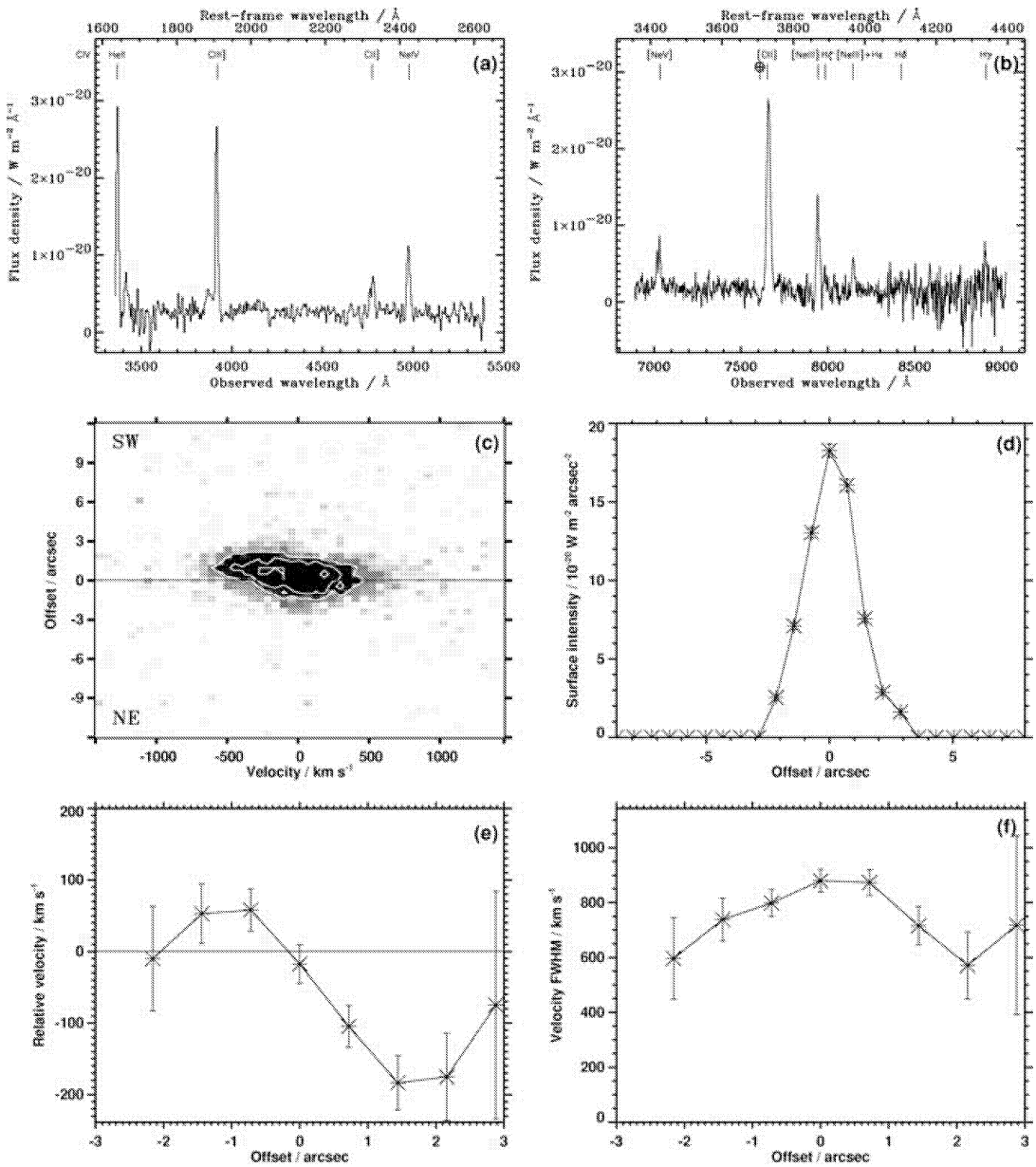

Figure 4. Spectroscopic data for 6C 1017+37. Offset directions are as labelled in (c). Contour levels in (c) are for 50, 75 and 100 per cent of the maximum surface brightness level. Other details as in Fig. 1.

sources ($D_{\rm rad} \gtrsim 120$ kpc) and shock-ionized sources ($D_{\rm rad} \lesssim 120$ kpc). To investigate these variations in the emission-line spectra with radio size, composite spectra for several different combinations of sources have been created, in addition to the spectra displayed in Fig. 11. This uses the same weighting system as for the combination of seven 6C galaxies, scaling the spectra of all sources by their continuum flux, weighted by the signal-to-noise ratio level of the continuum. The line ratios relative to [O II] for each of these sets of spectra can be found in Table 3. The data sets used consider the 3CR and 6C $z \sim 1$ subsamples both together and separately; these groups are further subdivided by radio source size (<120 kpc or >120 kpc). The C III] 1909 Å/[O II] 3727-Å ratio was calculated from the mean value within each subgroup of galaxies.

Fig. 12 shows the red and blue arm composite spectra for 21 6C and 3CR galaxies, separated into large (usually photoionized) sources and small (perhaps shock-ionized) sources. There are many differences between the two sets of spectra. Most emission lines in the small source composite spectra are fainter relative to [O II] than for the large source composite spectra, the Balmer lines being particularly weak in small sources. The ratio C III] 1909 Å/C II] 2326 Å is also considerably greater for the larger, photoionized sources.

In Fig. 13, the ratios of the emission-line fluxes of small and large sources are plotted against the ionization energy of each emission line, calculated as the difference in ionization energy between successive ionization states (e.g. for C III], the difference between the second and third ionization energies of carbon).[2] Ratios are plotted

[2]Ionization energies are taken from WebElements (http://www.webelements.com/) and from NIST (http://physics.nist.gov/cgi-bin/AtData/main_asd).

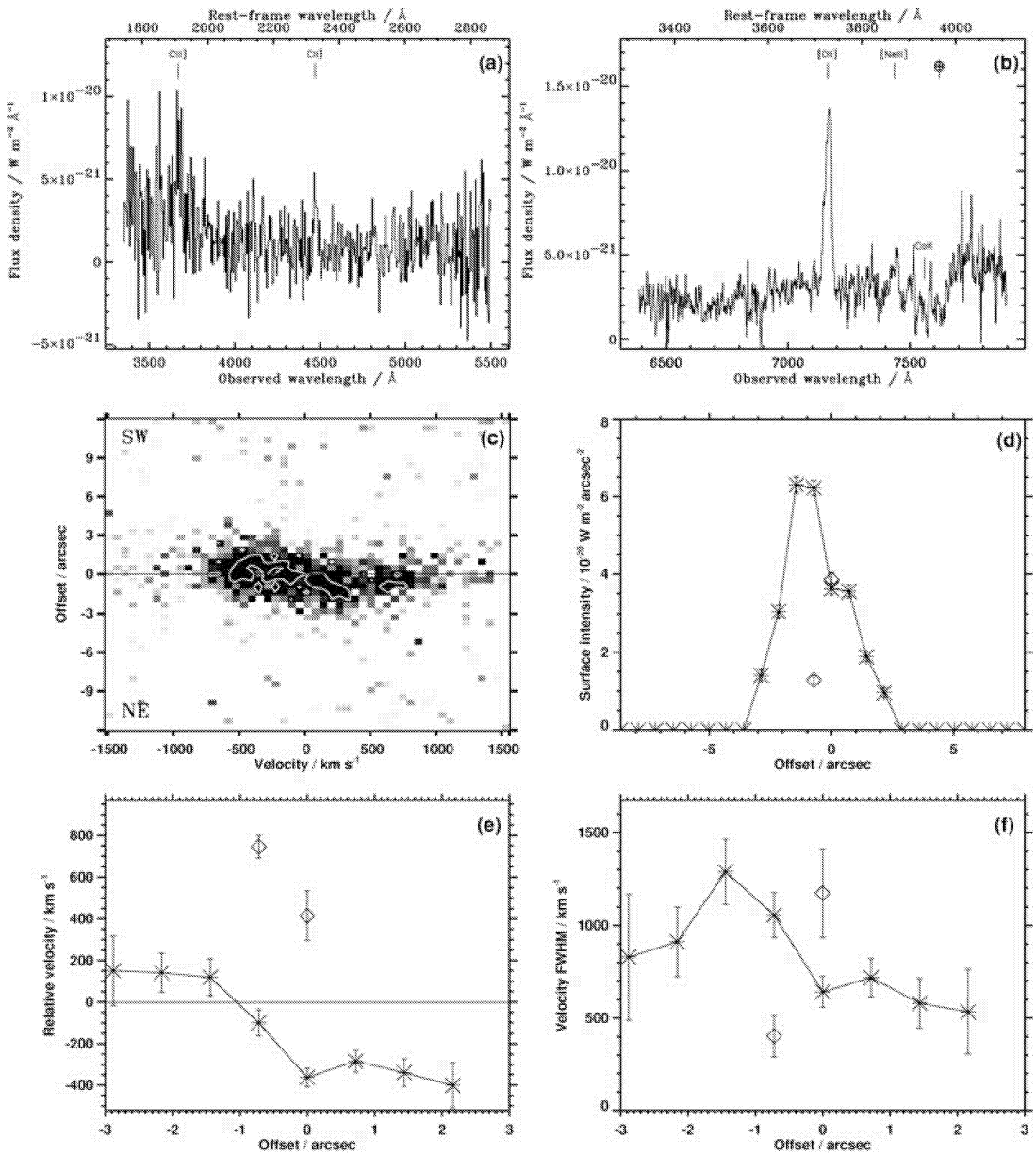

Figure 5. Spectroscopic data for 6C 1019+39. Contour levels in (c) are at 75 and 100 per cent of the maximum surface brightness level. For this object a second Gaussian was fitted to the data, which is plotted in the figures using open diamonds. Offset directions are as labelled in (c). Other details as in Fig. 1.

for the combined spectra of both 6C and 3CR sources. There is a clear anticorrelation of small/large source flux ratio with ionization state (95 per cent significant for the combination of 6C and 3CR galaxies), which clearly demonstrates the change in ionization state with radio size.

4.2 Ionization of the extended emission-line regions

The 6C subsample is well suited for comparison with the 3CR subsample studied by Best et al. (2000a,b). Both samples cover a narrow range of redshift at $z \sim 1$, whilst the 6C sources are approximately six times lower in radio luminosity than the 3CR galaxies. This enables a direct investigation of the effects of radio power on the emission properties of radio galaxies to be made.

Best et al. made use of a [Ne III] 3869 Å/[Ne V] 3426 Å versus C III] 1909 Å/C II] 2326-Å line diagnostic diagram to investigate the ionization mechanisms occurring within their subsample. Complete line ratio information was available for nine of the 14 galaxies, and these nine sources clearly fall into either of two regions on the diagnostic diagram. The two regions are well matched to the theoretical predictions of shock ionization and photoionization models, with sources smaller than 115 kpc appearing shock-ionized and larger sources lying in the AGN photoionization region of the plot. Fast radiative shocks can also be a strong source of ionizing photons; this can profoundly affect the ionization state of the emission-line regions, and is included in the shock models used in comparison with our data. Throughout this paper, the phrase 'shock ionization' generally refers to the models including this additional photoionizing component. A plot of the emission-line ratio (C III] 1909 Å/C II] 2326 Å) against radio size showed a clear correlation between the two parameters, significant at the 98.5 per cent level. The interpretation of these results was that the ionization state of

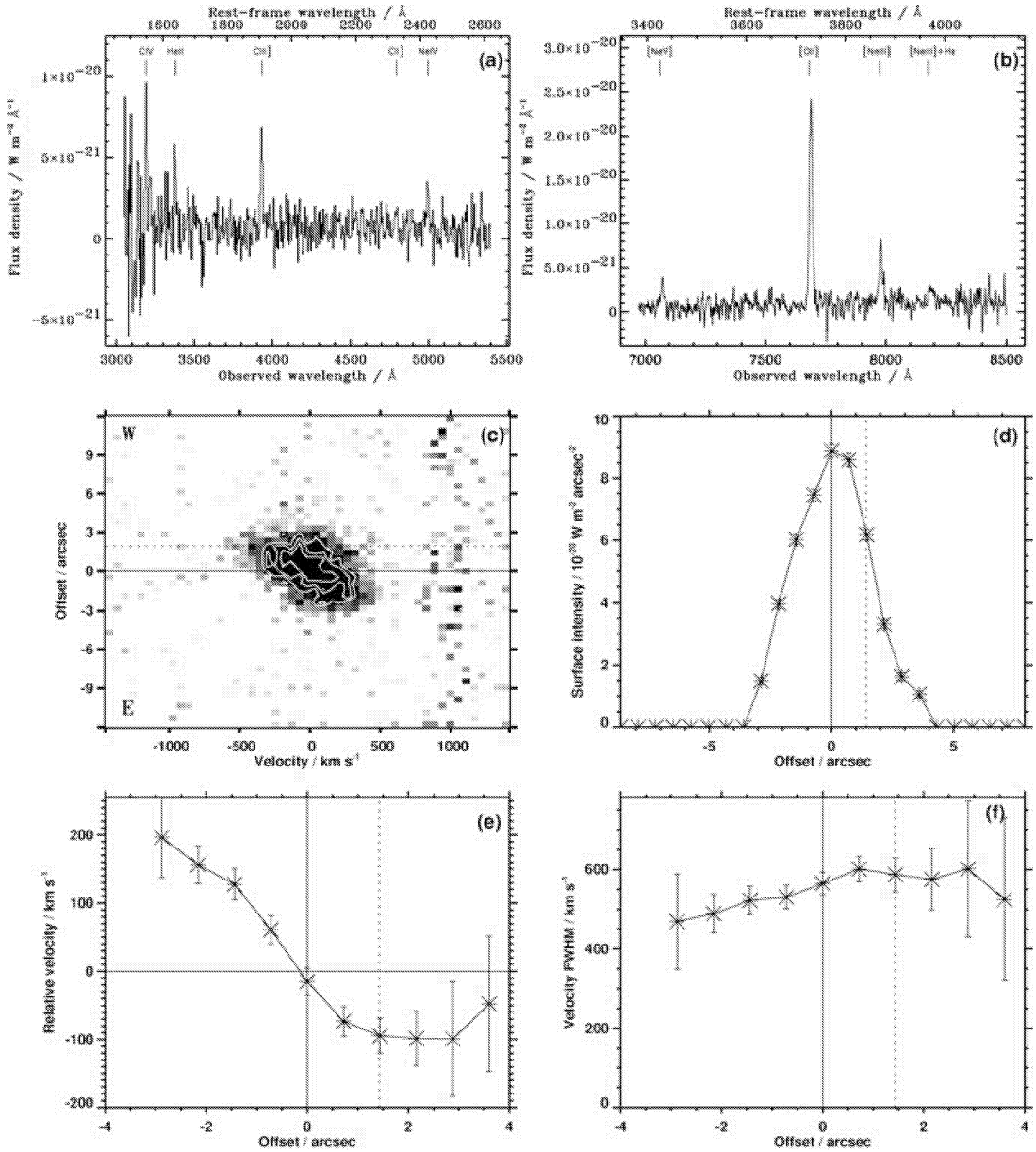

Figure 6. Spectroscopic data for 6C 1129+37. Contour levels in (c) are at 60, 75 and 90 per cent of the maximum surface brightness level. Offset directions are as labelled in (c). The solid line at offset zero represents the position of the eastern galaxy, tentatively identified as the host of the radio source. The position of the western galaxy is represented by the dotted line. Other details as in Fig. 1.

the emission-line gas varies strongly with radio size, and that the dominant ionization mechanism is photoionization for large radio sources ($D_{\rm rad} > 120$ kpc) and shock ionization for smaller sources ($D_{\rm rad} < 120$ kpc). The equivalent widths of the [O II] 3727-Å line are greater in size for small sources, and their continua also appear somewhat brighter on average. For the nine sources with complete line ratio data, a comparison of the average integrated flux of the [O II] line for photoionized and shock-ionized sources suggested that the power of the [O II] line is boosted in smaller, shocked sources.

Fig. 14 shows the line ratio diagnostic diagram of Best et al. (2000b) including the theoretical predictions and 3CR data. To this we have added the results obtained from our 6C subsample, as tabulated in Table 4. Whilst the 3CR galaxies marked on the line diagnostic diagram fall neatly into the two well-defined regions of either shock ionization or photoionization, the same cannot be said for the 6C galaxies. Based on radio source size, 6C 0943+39, 6C 1019+39, 6C 1011+36, 6C 1256+36 and 6C 1257+36 lie within the 'expected' regions on the diagnostic plot. The position of 6C 1129+37 (a radio source of intermediate size) is unusual, located a fair distance from the major group of photoionized sources. However, imaging observations of this source suggest that it may be interacting with a nearby companion galaxy (Inskip et al., in preparation). The small radio source 6C 1017+37 lies between the predictions of photoionization and shock ionization models. Although the size versus emission-line ionization mechanism relationship for the 6C galaxies is not as clear as for the 3CR galaxies, there is a similar trend. The photoionization models of Binette, Wilson & Storchi-Bergmann (1996) also appear to fit the data fairly well;

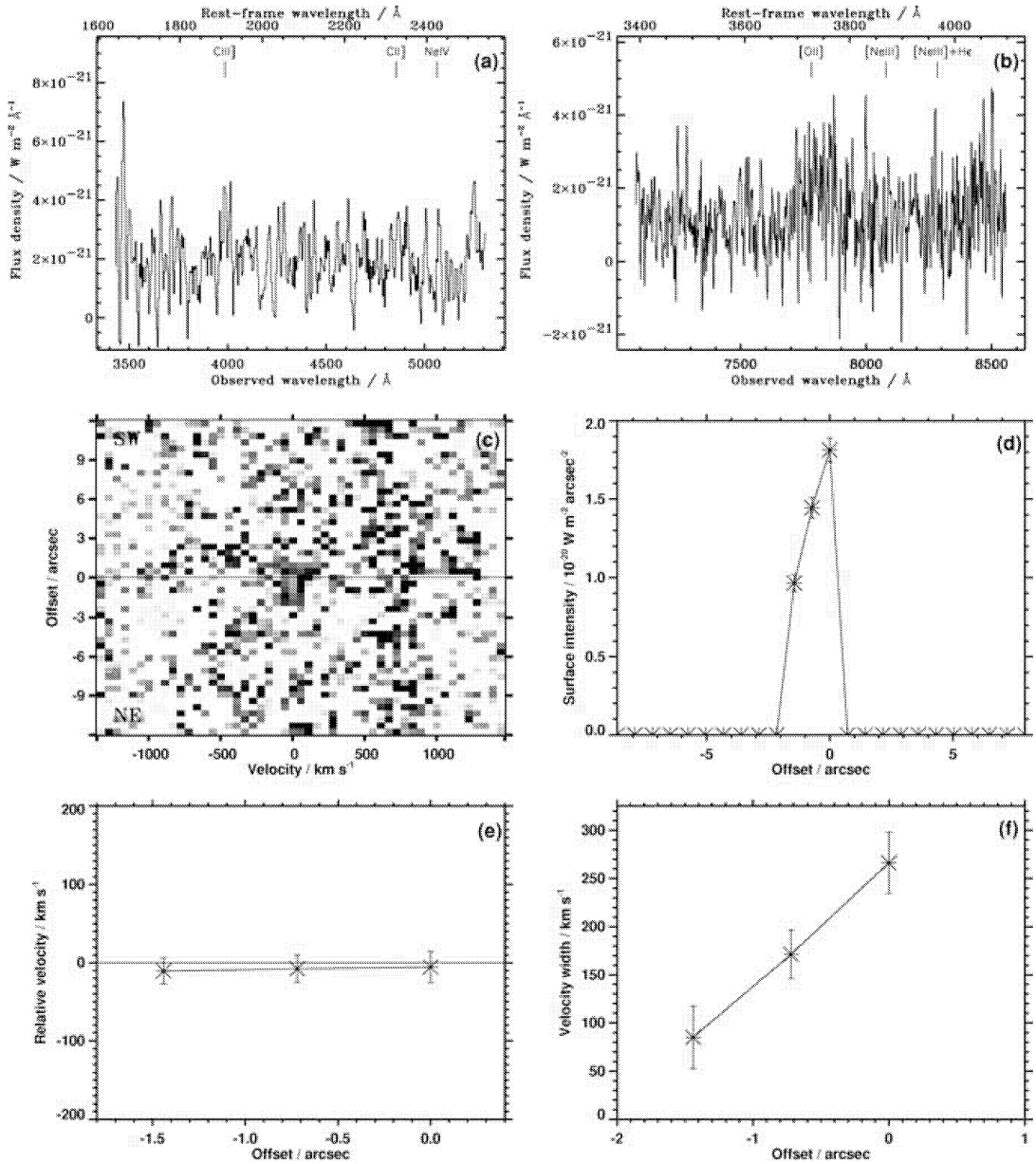

Figure 7. Spectroscopic data for 6C 1217+36. Offset directions are as labelled in (c). Other details as in Fig. 1. The [O II] emission line in this source is particularly faint.

further diagnostic plots utilizing other line ratios are required in order to determine the most appropriate models.

In Fig. 15 the carbon line ratio is plotted against radio size for the galaxies in both subsamples. These are very strongly correlated at the 99 per cent significance level using a Spearman rank correlation test (see Table 5) for all galaxies in both samples, at the 99 per cent level for 3CR galaxies alone and less strongly at the >75 per cent level for the 6C sources alone. The trend in ionization state is present for both samples, although somewhat weaker for the smaller subsample of 6C sources. This same trend is observed at higher redshifts: de Breuck et al. (2000) find that the C III] 1909 Å/C II] 2326-Å line ratio is correlated with radio size for their sample of higher redshift galaxies. The observed increase in C III] 1909 Å/C II] 2326 Å with radio source size is also mirrored by the results of Jarvis et al. (2001) at $z > 2$, for which composite spectra have been made for sources >70 and <70 kpc in radio size. These spectra clearly show a marked increase in the C III] 1909 Å/C II] 2326-Å line ratio in the larger sources. Stern et al. (1999) provide a composite spectrum for 13 high-redshift ($1.25 < z < 3.6$) radio galaxies, selected from the MIT Green Bank (MG) survey. These sources have flux densities intermediate between the 6C and 3CR sources at those redshifts, and radio sizes <90 kpc. The C III] 1909 Å/C II] 2326-Å line ratio for these galaxies is 1.2, which matches the values obtained for the smaller 6C and 3CR sources, and fits the predictions of the shock ionization models plotted on Fig. 14. It is also interesting to compare these line ratios with those of radio-quiet quasars (QSOs), which do not possess radio jets and so their emission-line spectra should be dominated by photoionization from the AGN. Composite spectra for QSOs show C III] 1909 Å/C II] 2326-Å line ratios of 5.3 (Boyle 1990) and 5.0 (Francis et al. 1991), indeed as expected for AGN

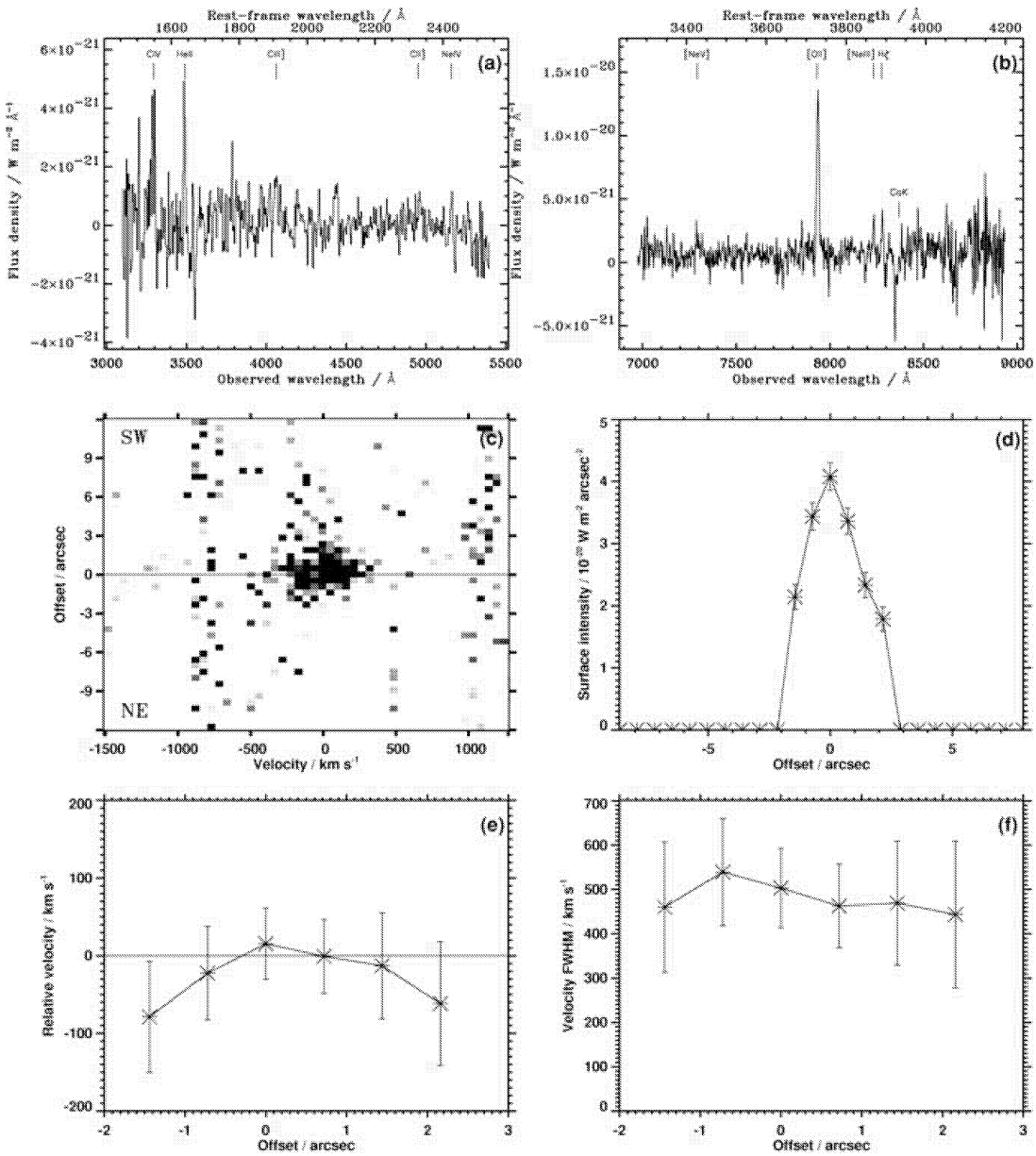

Figure 8. Spectroscopic data for 6C 1256+36, with the slit aligned along the radio axis (40°). The 2D [O II] spectrum combines data from the relatively close sky PAs of 40°, 0° and 22°. Offset directions are as labelled in (c). Other details as in Fig. 1.

photoionization and comparable to the values obtained for large 6C and 3CR radio sources.

4.3 Morphological and kinematical properties of the emission-line gas

The 3CR galaxies studied by Best et al. displayed some distinctive kinematic characteristics:

(i) The velocity width of the 3CR galaxies was shown to be strongly anticorrelated with radio size at greater than the 99 per cent significance level.

(ii) Small radio sources, defined as having a projected linear size less than 150 kpc, generally have more distorted velocity profiles than their larger counterparts, which have velocity profiles consistent with rotation. The number of separate velocity components was quantified by the parameter N_v, defined as the number of single gradient velocity components required to fit the velocity profile along the slit direction. This parameter displayed a clear variation with radio size, with all but one of the small radio sources having values $N_v > 1$ (distorted velocity profiles), and six out of seven of the larger sources having $N_v = 1$ (quiescent rotation-like profiles). χ^2 testing showed that the probability of this occurring by chance was less than 1 per cent.

(iii) The emission-line regions of small radio sources are greater than those of larger sources.

These results can be explained by the effects of shocks passing through the emission-line gas in the smaller sources, and show a direct connection between the ionization and kinematical properties of the emission-line regions of these galaxies. The equivalent kinematic properties of the eight 6C radio galaxies are tabulated in Table 4, namely the integrated [O II] emission-line intensity and

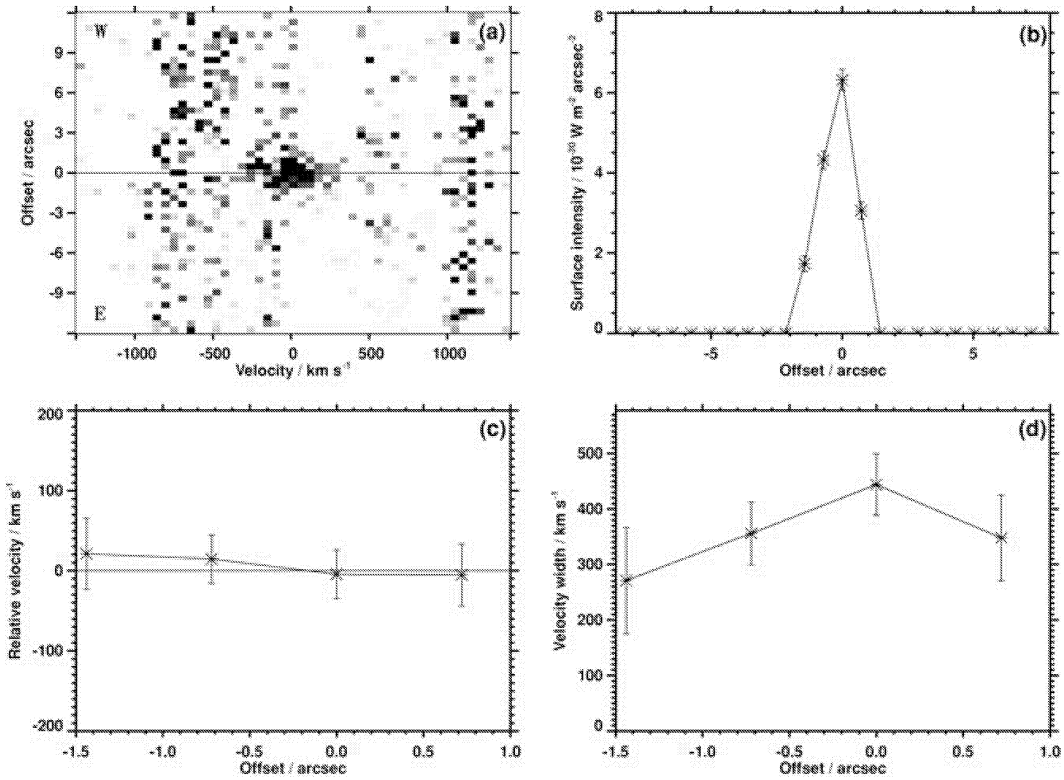

Figure 9. Spectroscopic data for 6C 1256+36, using data combined from observations at sky PAs of 79° and 115°. Offset directions are as labelled in (a). Other details as in Fig. 3.

equivalent width, the projected size of the emission-line region, the maximum FWHM, the range in relative velocities and the number of discrete velocity components observed in the [O II] line. We have investigated how well the relations found for the 3CR subsample also hold true for the less powerful sample of eight 6C radio galaxies. The significance of any correlations found is tabulated in Table 5.

Fig. 16(a) displays the dependence of N_v on radio size for the 6C galaxies currently investigated, and Fig. 16(b) the 3CR galaxies of the matched sample previously studied by Best et al. The 6C galaxies follow the same trend as those in the 3CR subsample: a χ^2 analysis of the data shows that the probability that this distribution occurs by chance is less than 1 per cent for the 6C sample, and less than 0.1 per cent for both samples combined (Table 5).

The 6C galaxies are also indistinguishable from the 3CR galaxies in their variation of maximum velocity FWHM with radio size (Fig. 17). An anticorrelation of FWHM with ionization state, as quantified by the C III] 1909 Å/C II] 2326-Å ratio, is also found. Another parameter that behaves similarly with radio size for both 3CR and 6C sources is the measured range in velocities observed in the [O II] line (Fig. 18). This is defined as the difference between the most positive and negative velocity components of the [O II] 3727-Å line as shown in Figs 1 and 10(e), excluding all data points with uncertainties greater than 100 km s^{-1}. On the whole, the velocity range data are weakly anticorrelated with radio size. 3C 265 (the isolated point at the top right corner of Fig. 18) possesses a very bizarre optical morphology (Best, Longair & Röttgering 1997). The observed morphology and high-velocity gas may be due to a cooling flow or the aftermath of a galaxy merger, although the exact nature of this source remains a mystery. With the exception of this unusual source, there is a clear tendency for larger sources to have a narrower range of velocities than smaller sources. However, the first difference between the two samples appears in this diagram. The lower radio power 6C galaxies appear to be restricted to a narrower, less extreme range of velocities than the more powerful 3CR sources, at all radio sizes. Kolmogorov–Smirnov testing of these trends shows that the differences observed (between large and small sources, and between the two samples) are statistically significant at only the 74 and 51 per cent levels respectively. A larger sample would be required to confirm (or disprove) the statistical significance of this result. Velocity range is also positively correlated with the FWHM of the emission-line gas at the 90 per cent significance level for the combination of both samples.

Fig. 19 displays the variation of the [O II] line luminosity ($L_{[O\,II]}$) with radio size for both samples. This is more appropriate than the [O II] equivalent width (used by Best et al.) for the 6C galaxies, for several reasons. Owing to the extremely low flux levels of the continua of the 6C galaxies, the measurements of the [O II] line equivalent widths are subject to large uncertainties. Also, the 3CR data show considerable boosting of the line flux of the smaller, shock-ionized sources. This effect seems more important in the 6C sources, especially 6C 1217+36 and 6C 1019+39, which have particularly low equivalent widths. More importantly, if we wish to compare the 3CR and 6C sources, we need to take into account the fact that there is roughly a factor of 5 difference in radio power between 3CR and 6C galaxies.

Rawlings & Saunders (1991) showed that radio jet kinetic power is strongly correlated with narrow-line luminosity in radio sources. Baum & Heckman (1989) find a strong correlation between radio and narrow-line luminosities. Jarvis et al. (2001) and Willott et al. (1999) also provide evidence for a positive correlation between these luminosities; their results suggest that this relation is close to

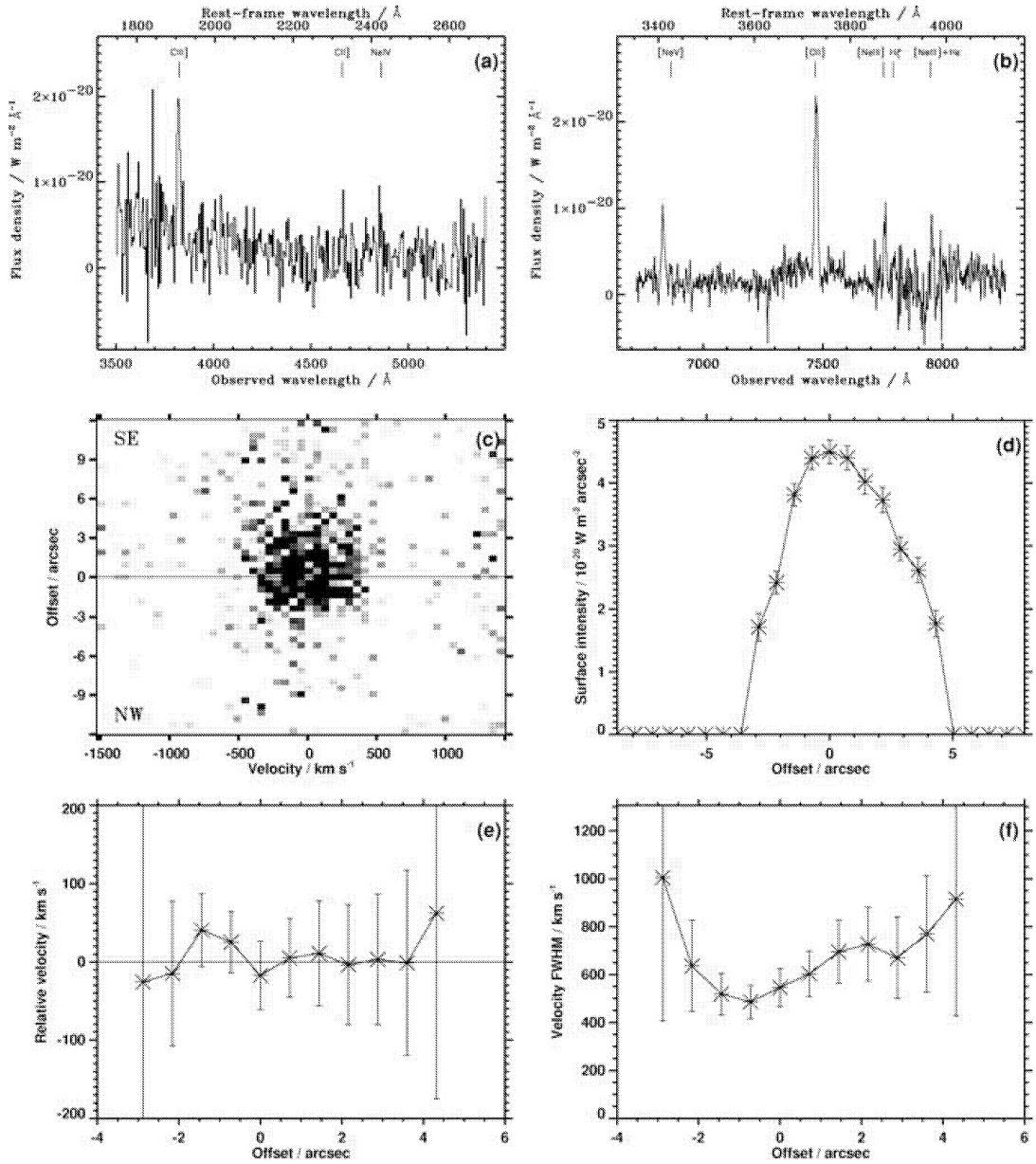

Figure 10. Spectroscopic data for 6C 1257+36. Offset directions are as labelled in (c). Other details as in Fig. 1.

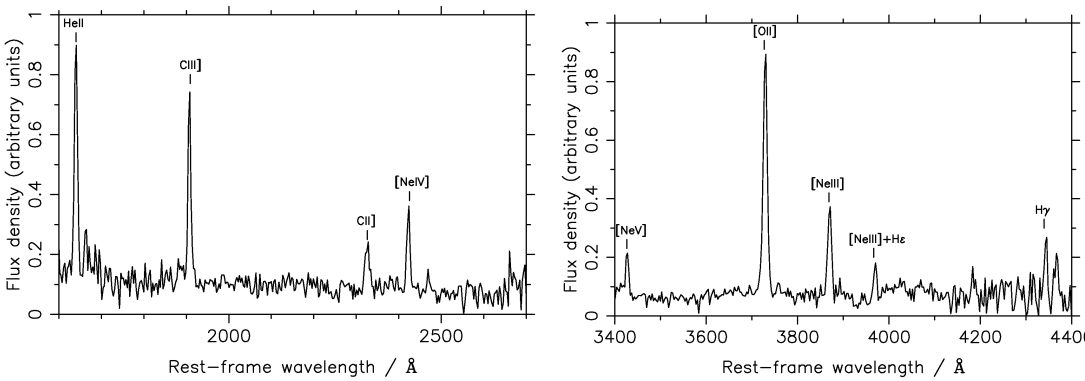

Figure 11. Red and blue arm composite spectra for the seven 6C galaxies.

Table 3. Emission-line fluxes and associated errors (relative to [O II] 3727 Å = 100) of the 'average' spectra for nine different galaxy groupings. Galaxies are grouped by sample (6C galaxies, 3CR galaxies, or all galaxies) and by radio size (large sources have $D_{\rm rad} \geqslant 120$ kpc). Also tabulated is the scatter in the data, included only when more than three measurements of a line are available within a particular group of sources. This is defined as the standard error on the mean value of the scaled line flux for each group. The final two rows give the C III] 1909 Å/C II] 2326 Å and [Ne III] 3869 Å/[Ne V] 3426-Å line ratios for the nine different groupings of sources.

Line		3CR	Small 3CR	Large 3CR	6C	Small 6C	Large 6C	All	All small	All large
C IV 1549 Å	Flux	44	42	–	91	–	92	45	36	61
	Error	6.4	6.1	–	13	–	13	6.9	6.0	9.5
	Scatter (%)	–	–	–	24	–	–	26	–	–
He II 1640 Å	Flux	42	36	58	57	–	70	31	31	43
	Error	6.2	5.2	10	8.3	–	11	4.7	4.8	7.3
	Scatter (%)	24	–	–	24	–	–	17	27	14
C III] 1909 Å	Flux	26	23	32	43	42	52	22	22	29
	Error	3.7	3.3	4.8	6.2	6.1	7.9	3.1	3.4	4.3
	Scatter (%)	18	16	30	20	–	–	17	16	22
C II] 2326 Å	Flux	8.4	8.7	7.1	14	16	7.5	7.1	8.4	6.7
	Error	1.4	1.7	1.1	2.3	2.4	4.1	1.1	2.5	1.5
	Scatter (%)	22	27	24	33	–	–	18	28	20
[Ne IV] 2425 Å	Flux	10	6.0	23	20	15	31	9.1	6.2	20
	Error	1.7	1.3	3.4	5.2	2.3	4.9	1.4	2.4	3.2
	Scatter (%)	27	33	32	24	–	–	19	27	24
Mg II 2798 Å	Flux	17	17	11	23	–	51	14	15	12.4
	Error	2.7	2.6	6.3	5.0	–	11	2.1	4.0	3.5
	Scatter (%)	35	–	–	–	–	–	25	31	38
[Ne V] 3426 Å	Flux	–	–	–	14	14	19	11	9.5	14
	Error	–	–	–	2.3	2.4	4.2	1.6	2.5	2.3
	Scatter (%)	–	–	–	23	–	–	21	33	–
[O II] 3727 Å	Flux	100	100	100	100	100	100	100	100	100
	Error	10	10	10	10	10	10	10	10	10
	Scatter (%)	19	22	19	29	–	–	17	20	20
[Ne III] 3869 Å	Flux	24	21	47	30	28	31	27	22	34
	Error	3.4	3.0	6.8	4.3	4.2	5.3	3.8	3.7	4.8
	Scatter (%)	18	27	19	27	–	–	15	23	17
Hζ 3889 Å	Flux	3.3	3.8	8.4	–	–	5.1	4.3	–	5.6
	Error	0.7	0.9	1.5	–	–	3.8	0.6	–	1.3
	Scatter (%)	17	17	26	–	–	–	16	–	24
Hϵ + [Ne III] 3967 Å	Flux	10	10	14	7.1	3.9	16	12	7	18
	Error	1.5	1.4	2.1	1.4	2.5	4.7	1.7	1.8	3.4
	Scatter (%)	17	21	22	18	–	–	15	19	18
[S II]	Flux	2.4	2.4	3.9	–	–	–	2.8	3	4.5
	Error	1.2	1.4	2.7	–	–	–	1.7	2.0	2.4
	Scatter (%)	–	–	–	–	–	–	–	–	–
Hδ 4102 Å	Flux	8.1	7.0	12	–	–	–	9.1	6.8	11
	Error	1.7	1.4	2.5	–	–	–	2.3	2.0	3.0
	Scatter (%)	14	–	20	–	–	–	16	13	21
Hγ 4340 Å	Flux	14	11	31	9.0	4.9	18	19	13	26
	Error	2.0	1.8	3.4	5.0	2.7	9.7	2.8	4.1	6.6
	Scatter (%)	22	37	23	–	–	–	18	30	21
[O III] 4363 Å	Flux	2.4	3.6	3.9	–	–	–	9.4	4.6	11
	Error	1.5	2.3	2.7	–	–	–	2.2	2.2	6.2
	Scatter (%)	–	–	–	–	–	–	–	–	–
C III] 1909 Å/C II] 2326 Å		3.10	2.64	4.51	3.07	2.63	6.93	3.10	2.62	4.33
Error		0.68	0.64	0.97	0.67	0.55	3.93	0.65	0.88	1.16
[Ne III] 3869 Å/[Ne V] 3426 Å		–	–	–	2.14	2.00	1.63	2.45	2.32	2.43
Error		–	–	–	0.47	0.46	0.46	0.50	0.72	0.53

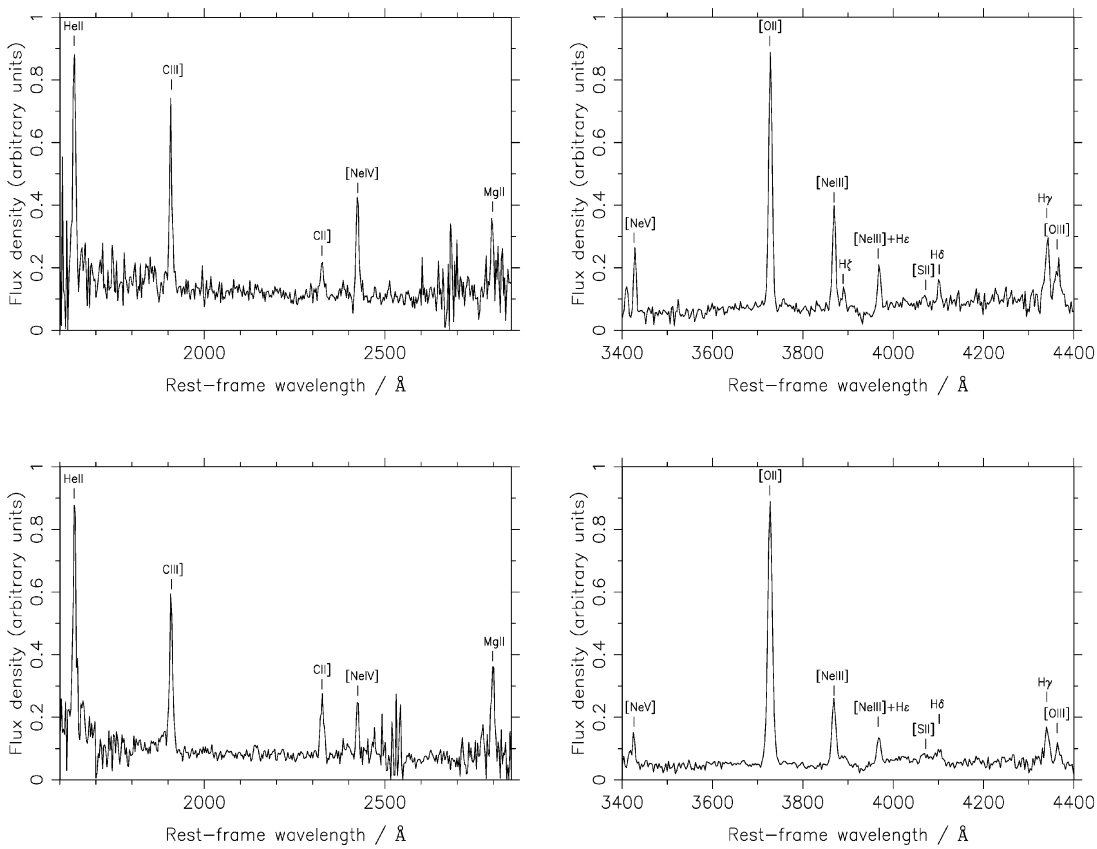

Figure 12. Composite red and blue arm spectra for both 6C and 3CR galaxies combined: (top) large (>120 kpc) radio sources; (bottom) small (<120 kpc) radio sources. The former display many characteristics of photoionized regions, while the latter spectra are more typical of shock ionization.

being a proportionality, although the exact slope is still unclear. From this correlation, the line emission of the 6C galaxies is expected to be significantly weaker than that of more powerful 3CR galaxies. However, the relation of continuum emission to radio power is not so well known. Without this, we cannot gauge the reliability of comparing equivalent widths of two data sets at different radio powers, and so we compare the luminosities instead. In order to be able to compare the two samples directly, Fig. 19(b) shows the line luminosity of each source scaled by the ratio of the host galaxy's radio flux density at 151 MHz to that of the average for the 3CR subsample. Assuming that radio and narrow-line luminosities are proportional, this removes to first approximation the decrease in $L_{[\mathrm{O\,II}]}$ in the 6C sources due to the difference in radio power between the two subsamples. The resulting [O II] line luminosities of galaxies from both samples occupy a narrow range of values, and are anticorrelated with radio size. This anticorrelation is significant at the 97 per cent level for the 6C subsample alone, at 94 per cent for the 3CR subsample alone, but at greater than the 99 per cent significance level when the samples are combined.

Interpretation of the *P–D* relation (Scheuer 1974; Baldwin 1982) for radio galaxies predicts that, for an assumed constant AGN output, the radio luminosity of a source will decrease monotonically over its lifetime (Kaiser, Dennett-Thorpe & Alexander 1997). If two sources are observed to have identical radio luminosities, the larger source of the two will host an intrinsically more powerful AGN, and thus produce more luminous [O II] emission due to the strong correlation between radio power and emission-line luminosity. By scaling our data to the same radio luminosity, we can expect the prediction of greater emission-line luminosity for larger, more powerful sources to reduce the strength of any intrinsic correlation between $L_{[\mathrm{O\,II}]}$ and radio source size/age. The observed anticorrelation therefore provides a lower limit to the strength of the actual anticorrelation between $L_{[\mathrm{O\,II}]}$ and radio source age.

An examination of the line intensity versus spatial offset plots for the 6C galaxies, in contrast to the equivalent plots for 3CR sources by Best et al. (2000a), shows that fits to the [O II] emission lines of 6C galaxies generally result in a more steeply edged line intensity profile. This is a result of the much lower S/N in the 6C spectroscopic data, despite the longer integration times of the observations. We are unable to fit Gaussians to the extracted 2D [O II] 3727-Å emission line out to the same spatial extent as would have been possible with higher signal-to-noise ratio data, and, as this is the method by which we determined the spatial size of the emission-line regions, comparing different EELR sizes within each of the two data sets is not straightforward.

To overcome this problem, we added noise to the 2D region about the [O II] 3727-Å emission line for 3CR sources, reducing the S/N to a level equivalent to that observed in the 6C sources. By determining the spatial extent of the region in which fits to the [O II] line could be made in this noisier version of the spectra, we estimated the amount by which the size of the emission-line regions in 6C sources may have been underestimated. Typically, the addition of noise to the 2D 3CR spectra resulted in a reduction in the deduced size of the emission-line region of between 15 and 30 per cent. Fig. 20 plots emission-line region size versus radio size, after the former has been scaled up by 25 per cent for the 6C sources. It can be seen

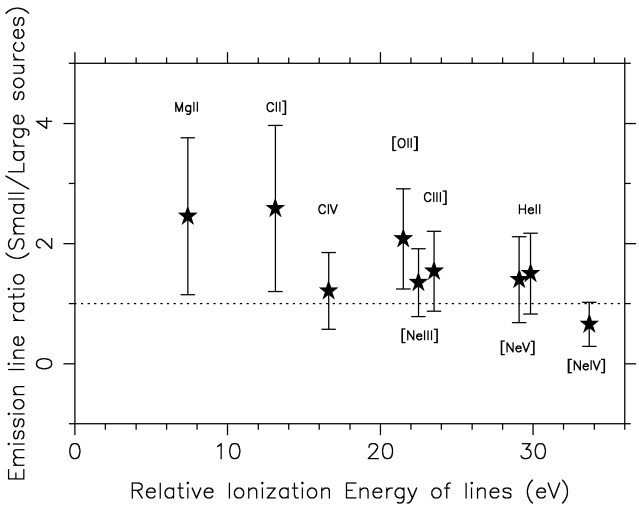

Figure 13. Plot of small-to-large source emission-line flux ratio versus ionization energy of the emission lines, calculated as the difference in ionization energy between successive ionization states. The stars represent the results for both 6C and 3CR sources.

that, after accounting for this reduced S/N of the 6C sources, the relation between emission-line region size and radio size for these galaxies is in agreement with that found by Best et al. for the 3CR subsample. We also see that the size of the emission-line region is strongly correlated with the range of velocities observed in the emission-line gas for the combination of the two samples, although only weakly for the 6C sources alone. The lack of an anticorrelation in the 6C data is due in part to the position of 6C 1257+36 on Fig. 20, which may perhaps be currently undergoing a jet–cloud interaction, and this may explain its larger than expected EELR size.

One other point to note is that the 2D extracted spectra of the [O II] 3727-Å lines which have the most distorted profiles, seemingly indicative of shocks, occur only in the galaxies whose ionization states place them in the shock region of the line diagnostic diagram. We also see that the smoothly profiled sources occupy the photoionization region of the plot. The small radio source 6C 1017+37 has a large emission-line region, typical for its radio size, but has a very smooth profile more like that found in the larger, photoionized radio galaxies. This source lies within the photoionization region of the emission-line diagnostic plot. Although radio source size is a fairly reliable indicator of ionization state (and perhaps ionization mechanism), the appearance of the [O II] 3727-Å line also appears to correlate with the best-fitting model of the ionization mechanism causing the excitation of the emission-line regions. This result also strongly suggests that the ionization and kinematic properties of the EELRs are fundamentally linked.

5 DISCUSSION

A consistent picture emerges from the analysis of the 3CR and 6C observations discussed in Section 4:

(i) The small radio sources ($D_{\rm rad} < 120$ kpc) have extensive emission-line regions with distorted velocity profiles, indicating multiple components present in the gas, and have line ratios consistent with the predictions of models for ionization by fast radiative shocks. Typically, these sources possess emission-line regions similar in size to the radio source, up to 100 kpc. The greater [O II] luminosities of these sources compared with the large radio sources is in part due to the increased size of their emission-line regions.

(ii) The larger radio sources ($D_{\rm rad} > 120$ kpc) have compact emission-line regions with smooth velocity profiles, and their emission-line ratios are well matched by the predictions of the Allen, Dopita & Tsvetanov (1998) models for photoionization by an obscured AGN. For these sources photoionized gas is observed out to similar extents from the AGN (~25 kpc) in both the 6C and 3CR samples, once the differing signal-to-noise ratios of the observations have been taken into account. The photoionization models which best fit the emission-line ratios of the less powerful 6C radio sources have on average lower ionization parameters (defined as the ratio of the number density of ionizing photons to the number density of the gas) than those found in the large 3CR sources.

Although it is evident that the two different types of excitation each dominate in a subset of the sources, Fig. 14 shows that the sources lie along a continuous sequence in the line ratio diagram, and it is almost certain that both processes play a role in the majority of the sources, with the balance between the two changing with radio size.

5.1 The ionization and structure of the photoionized extended emission-line regions

For large, photoionized radio sources, the total emission-line flux scales with radio power for the two samples (Fig. 19) and the physical extents of the emission-line regions are comparable (~25 kpc) at different radio powers. These results can be accounted for if the clouds making up the EELR are ionization-bounded with a small covering factor; their minimum sizes can then be estimated using the expression for the Hβ line luminosity given by Osterbrock (1989):

$$L_{\rm H\beta} = h\nu_{\rm H\beta}\frac{\alpha^{\rm eff}_{\rm H\beta}(H^0,T)}{\alpha_{\rm B}(H^0,T)}\int_{\nu_0}^{\infty}\frac{L_\nu}{h\nu}\,{\rm d}\nu\,,$$
$$= n_{\rm e}n_{\rm p}\alpha^{\rm eff}_{\rm H\beta}h\nu_{\rm H\beta}V\epsilon,$$

where $\alpha^{\rm eff}_{\rm H\beta}(H^0,T)$ and $\alpha_{\rm B}(H^0,T)$ are the recombination coefficients for the Hβ line and the total recombination rate, V is the total volume and ϵ is the filling factor ($\epsilon = 1$ for an individual cloud).

If the flux of ionizing photons reaching the cloud gives an ionization parameter U, $Ucn_{\rm p} = \int_{\nu_0}^{\infty}(L_\nu/h\nu)\,{\rm d}\nu$. Then, the depth to which the cloud would be fully ionized would be $d = Uc/n_{\rm e}\alpha_{\rm B}(H^0,T)$. Taking $\log_{10}U = -1$ (from the analysis of the photoionized galaxies as plotted on Fig. 14) and $T \sim 10^4$ K, the minimum size of an ionization-bounded cloud would be $d \sim 37.5(10^8\,{\rm m}^{-3}/n_{\rm e})$ pc. These figures are consistent with the standard picture in which the photoionized clouds occupy only a small fraction of the observed emission-line region.

5.2 Radiative shocks in small radio sources

The emission-line ratios of sources with radio sizes $D_{\rm rad} < 120$ kpc can be explained by the predictions of the shock ionization models of Dopita & Sutherland (1996), in which certain emission lines are boosted by shock excitation. The changing line ratios as compared with photoionization models which successfully account for the spectra of the large sources are evidence that shock boosting is important in the small radio sources. For example, the C III] 1909 Å/C II] 2326-Å line ratio changes systematically with radio size. A similar trend is seen in the spectra of radio sources at much larger redshifts (de Breuck et al. 2000; Jarvis et al. 2001). Another characteristic of the spectra of the smaller radio sources, observed in

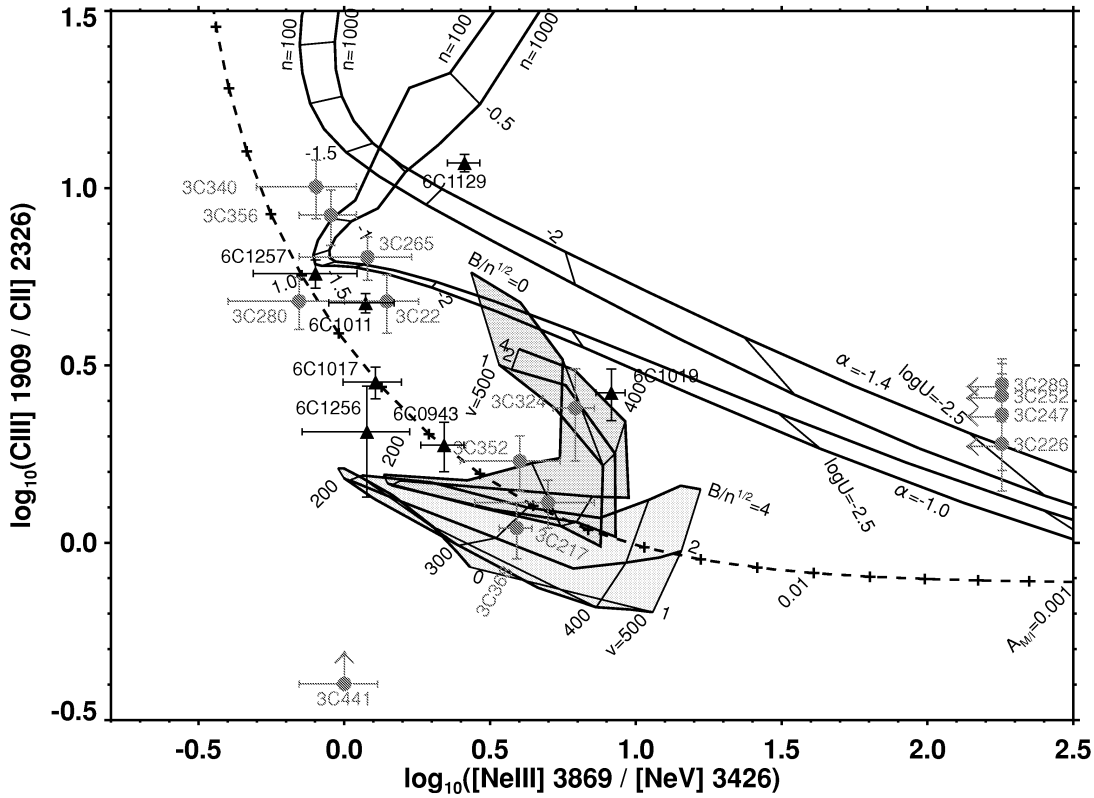

Figure 14. A carbon ratio versus neon ratio emission-line diagnostic plot for 6C (black triangular data points) and 3CR galaxies (grey circular data points). For full details of how the theoretical lines were determined, see Best et al. (2000b) and references therein. The results are compared with the theoretical predictions for shock ionization, simple photoionization, and photoionization including matter-bounded clouds. The shock ionization line ratio predictions are those of the models of Dopita & Sutherland (1996). Results both for simple shock ionization (faint shading) and for models including a precursor ionization region (darker shaded region) are included on the diagram. The precursor ionization region is created by UV photons produced by the shock which have diffused upstream. Shock velocities were allowed to vary between 150 and 500 km s^{-1}. The 'magnetic parameter', $B/\sqrt{n}$ (which controls the effective ionization parameter of the post-shock gas), was varied from 0 to 4 μG cm$^{-1.5}$. The simple photoionization model tracks are taken from the theoretical line ratios of Allen et al. (1998), calculated using the MAPPINGSII code (Sutherland, Bicknell & Dopita 1993). A power-law spectrum illumination ($F_\nu \propto \nu^\alpha$, $\alpha = -1$ or -1.4, with a high-energy cut-off at 1.36 keV) of a planar slab of material (density $n_e = 100$ or 1000 cm^{-3}) was assumed, with an ionization parameter $10^{-4} \leqslant U \leqslant 1$. The models correspond to cloud sizes from 0.003 to 32 pc, and are ionization-bounded. Evans et al. (1999) consider the uncertainty in the models of Allen et al. and Dopita & Sutherland to be at a level of about 0.3 dex. Matter-bounded photoionization tracks are also plotted, using the predicted line ratios of Binette et al. (1996). Sources plotted at the edges of the diagram lack data for one of their emission-line ratios.

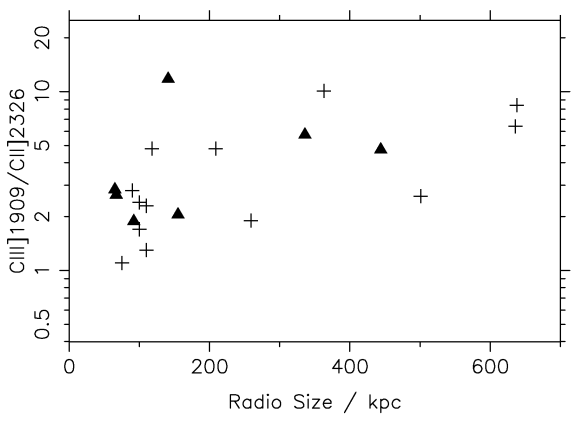

Figure 15. The correlation between C III] 1909 Å/C II] 2326 Å emission-line ratio and the projected linear size of the radio source. 6C galaxies are marked as filled triangles, and the 3CR galaxies studied by Best et al. are marked as crosses.

both $z \sim 1$ subsamples, is a reduction in Balmer line flux. Morse, Raymond & Wilson (1996) have noted that the high electron temperature produced by fast ionizing shocks reduces the efficiency of Balmer emission relative to emission by UV semi-forbidden lines and resonance lines, indicating that this result too is consistent with shock ionization playing an important role. Let us therefore study the physics and energetics of the shock excitation models in a little more detail, to consider whether or not the shock energetics are indeed sufficient to explain the observed properties of the emission-line regions.

In considering the effects of the shocks, we must first consider the properties of both the shock and the gas into which it is expanding. We consider (cf. review by McCarthy 1993) an elliptically shaped shock wave associated with the cocoon of the expanding radio source, propagating at a velocity of 0.01–0.03c through the ambient diffuse hot ($\sim 10^7$ to 10^8 K) gas surrounding a massive radio galaxy. Cool ($\sim 10^4$ K) dense clouds are embedded in the hot gas with very small filling factor ($\sim 10^{-6}$); these are in pressure equilibrium with the hot phase, implying a density ratio of $n_{\rm cloud}/n_{\rm IGM} \sim 10^3$ to 10^4. It is these cooler clouds that produce the line emission.

Table 4. Ionization and kinematic properties of the emission-line regions of the 6C radio galaxies. Column 1 gives the name of the radio source, and column 2 its redshift. The projected linear size of the radio source is tabulated in column 3. Columns 4 to 7 give the C III] 1909 Å/C II] 2326 Å and [Ne III] 3869 Å/[Ne V] 3426-Å emission-line ratios and their errors. Column 8 contains the integrated [O II] 3727-Å flux density, and column 9 its rest-frame equivalent width. The physical size of the emission-line region as determined from the extracted 2D image of the [O II] 3727-Å emission line is given in column 10. Columns 11 to 13 contain further information on the [O II] 3727-Å emission line: its maximum FWHM, the observed range in relative velocities along the slit, and the number of discrete velocity components.

Source	z	Radio size (kpc)	C III]/C II] ratio	C III]/C II] error	[Ne III]/[Ne V] ratio	[Ne III]/[Ne V] error	[O II] flux ($\times 10^{-19}$) (W m^{-2})	Eq. width (Å)	Emiss. size (kpc)	Max. FWHM (km s^{-1})	Vel. range (km s^{-1})	No. comps (N_v) (kpc)
(1)	(2)	(3)	(4)	(5)	(6)	(7)	(8)	(9)	(10)	(11)	(12)	(13)
6C 0943+39	1.036	92	1.885	0.30	2.200	0.37	5.01	211	68.4	860	305	2–3?
6C 1011+36	1.042	444	4.749	0.30	1.184	0.30	1.24	41	18.6	400	80	1
6C 1017+37	1.053	65	2.838	0.29	1.280	0.29	6.86	195	43.7	880	245	2
6C 1019+39	0.922	67	2.649	0.44	8.238	0.94	2.43	58	42.3	1300	475	3[a]
6C 1129+37	1.060	141	11.79	0.67	2.586	0.33	5.14	226	56.2	600	300	2?
6C 1217+36	1.088	38	1.208	1.02	1.000	1.22	0.51	59	12.6	265	20	1
6C 1256+36	1.128	155	2.055	0.71	1.196	0.48	2.09	147	31.6	660	40	1
6C 1257+36	1.004	336	5.750	0.52	0.797	0.31	2.24	83	61.7	775	60	1

[a] This source also contains a discrete high-velocity component.

Table 5. Correlation table. The values tabulated give the significance level of any correlation found using a Spearman rank test. An asterisk denotes correlations at a significance level of 75 per cent or less, and implies an uncorrelated pair of data sets. Positive and negative signs indicate whether a parameter set is correlated or anticorrelated, respectively. Also included are the probabilities of the results of the χ^2 analysis of the distribution of the N_v parameter as a function of radio size occurring by chance.

Parameters	3CR data			6C data excluding 6C 1217+36			All data excluding 6C 1217+36		
	r_S	n	prob. (%)	r_S	n	prob. (%)	r_S	n	prob. (%)
Carbon ratio vs. Radio size	0.681	13	+99.5	0.357	7	+78	0.523	20	+99.1
Maximum FWHM vs. Radio size	−0.650	14	−99.4	−0.821	7	−98.8	−0.667	21	−99.95
Carbon ratio vs. Maximum FWHM	−0.667	13	−99.4	−0.464	7	−85	−0.537	20	−99.3
EELR velocity range vs. Radio size	−0.282	14	−84	−0.631	7	−93.6	−0.330	21	−92.8
EELR velocity range vs. Maximum FWHM	0.408	14	+92.6	0.487	7	+87	0.480	21	+98.6
Scaled [O II] luminosity vs. Radio size	−0.437	14	−94.1	−0.757	7	−97.6	−0.528	21	−99.3
EELR size vs. Radio size	−0.286	14	−84	−0.286	7	*	−0.200	21	−81
[+25% size]	−0.286	14	−84	−0.286	7	*	−0.268	21	−88
Scaled EELR size vs. EELR velocity range	0.718	14	+99.8	0.288	7	*	0.578	21	+99.7
N_v distribution probability			<1%			<1%			<0.1%

The passage of highly supersonic shocks through the cool clouds can have a profound effect on their temperature, density and ionization state. The shock models of Dopita & Sutherland (1996) include the presence of magnetic fields to prevent excessive compression behind the shock, and predict that the shocked gas is compressed as $n_f/n = (8\pi \times 10^{-7} \mu m_H)^{1/2} V_s/(B/n^{1/2})$, which for magnetic flux densities of $B \sim 1$–5 nT, determined from estimates of the equipartition field strengths in the radio source cocoons, corresponds to a compression factor of $\sim 10^2$. Because of the compression of the gas, the ionization parameter for photoionization decreases. The effects of cloud compression or expansion alone cannot, however, account for the observed differences between the ionization states of large and small sources; for example, the reduction of $\log_{10} U$ from -1 to -3 that would be required for photoionization to account for the observed change in the C III] 1909 Å/C II] 2326-Å line ratio between large and small radio sources, would not be compatible with the changes in the observed [Ne III] 3869 Å/[Ne V] 3426-Å line ratio (the implied change in $\log_{10} U$ from this line ratio is ~ 0.7 to 1; see Fig. 14). Furthermore, excessive compression of the gas clouds could lead to collisional de-excitation. Since the critical density at which [O II] 3727 Å is collisionally de-excited is $\sim 10^{10}$ m^{-3} (Morse et al. 1996), the compressed gas cannot exceed this density.

The shock models of Dopita & Sutherland (1996), which assume that all the mechanical energy of the shock is radiated, provide a scaling relation for the total radiative luminosity per unit area of a shock,

$$L_T = 2.28 \times 10^{-6} \left(V_s / 100\,\mathrm{km\,s^{-1}}\right)^{3.0} (n/10^6\,\mathrm{m^{-3}})\mathrm{W\,m^{-2}}\,,$$

where V_s is the shock velocity and n the ambient density of the pre-shock gas. The shocks propagate at a much lower speed through the clouds than through the intercloud hot gas, because of their greater density. Assuming pressure balance, $V_{s,\mathrm{cloud}} \approx V_{s,\mathrm{IGM}} \sqrt{n_{\mathrm{IGM}}/n_{\mathrm{cloud}}}$ (Mendoza 2000), and so for a typical mean shock velocity of the cocoon of $0.02c$,[3] the velocity of the shock within a cloud is ~ 200 km

[3] Note that this mean velocity of the shock front is lower than the velocity at which the radio size increases, because the transverse radio shocks are slower by a factor of the aspect ratio of the radio source, typically 3–5. However, owing to the v^3 dependence the actual value assumed is decreased by a smaller factor than this.

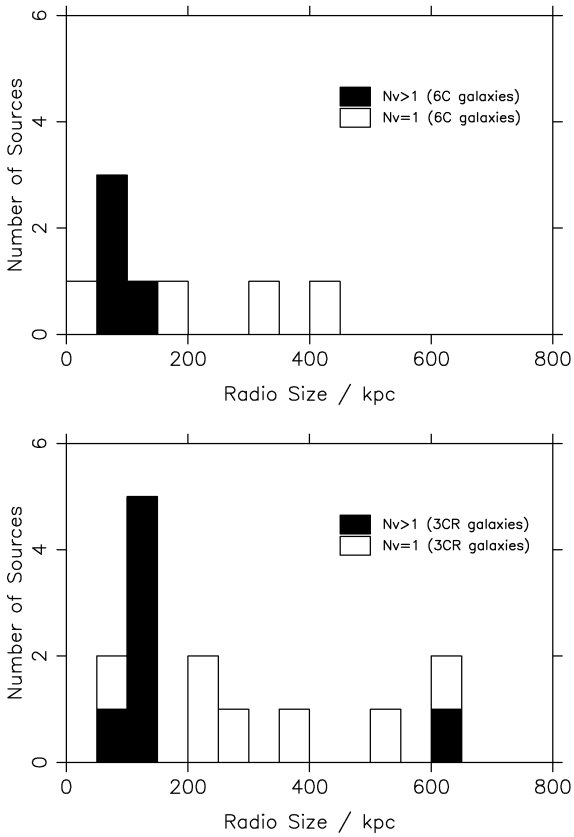

Figure 16. (a) The distribution of radio source sizes of 6C galaxies with smooth velocity profiles (white) and irregular velocity profiles (black). (b) The same results for the 3CR galaxies studied by Best et al. (2000b). The slight difference with respect to the diagram presented by Best et al. arises only from the different cosmology adopted in this paper.

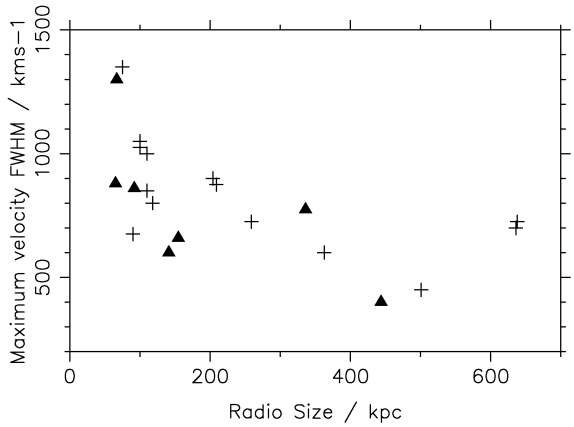

Figure 17. The inverse correlation between the maximum FWHM of the [O II] 3727-Å emission line and the projected linear size of the radio source. 6C galaxies are marked as filled triangles, and the 3CR galaxies studied by Best et al. are marked as crosses.

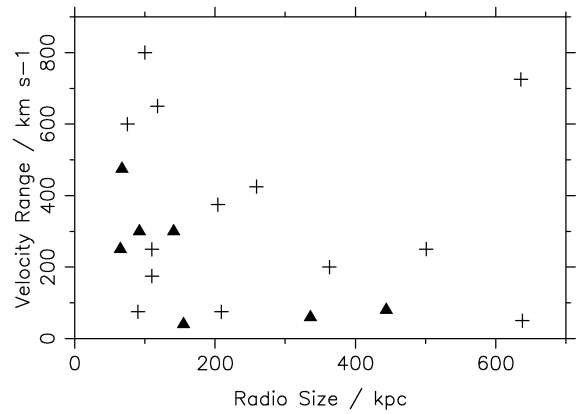

Figure 18. The variation of the velocity range observed for the emission-line region with the size of the radio source. 6C galaxies are marked as filled triangles, and the 3CR galaxies studied by Best et al. are marked as crosses.

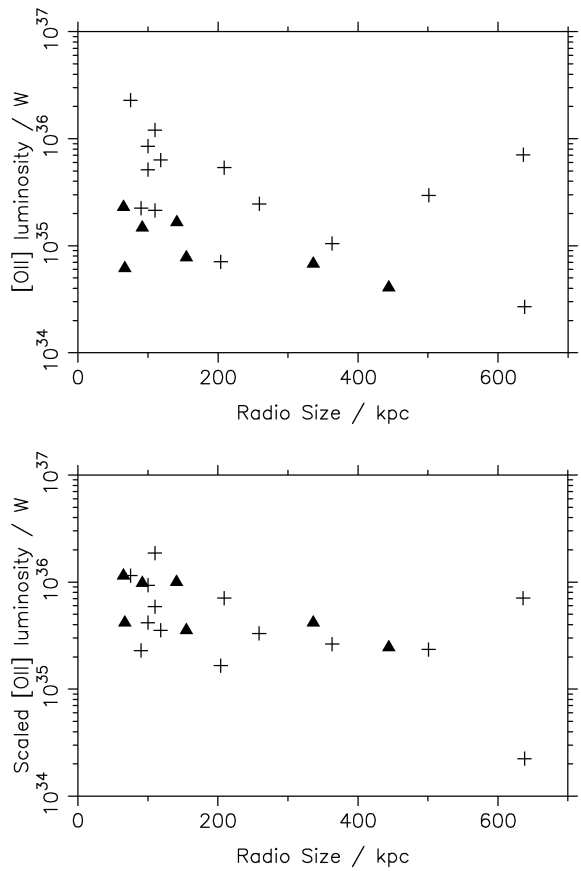

Figure 19. The variation of the luminosity of the [O II] 3727-Å emission line with the size of the radio source. (top) Unscaled line luminosities. (bottom) Line luminosities scaled by radio power at 151 MHz as a fraction of the average 3CR radio power. 6C galaxies are marked as filled triangles, and the 3CR galaxies studied by Best et al. are marked as crosses.

s^{-1}. This is within the range of values considered by the Dopita and Sutherland models.

The shocked gas cools on a time-scale of about 10^4 yr according to the Dopita and Sutherland models, very much shorter than the lifetime of a radio source. The direct ionization of the cool clouds by the passage of these shocks will therefore be a short-lived effect, and the associated boosting of emission-line luminosities will only be relevant for those clouds close to the bow shock. For a radio source of about 50 kpc size, assuming emission-line clouds of density $n_{\rm cloud} \sim 10^8$ m^{-3} with a volume filling factor of $\sim 10^{-6}$, the total radiative flux produced in the clouds by the direct passage of the shocks will be of the order of 10^{34} W. When compared to the [O II]

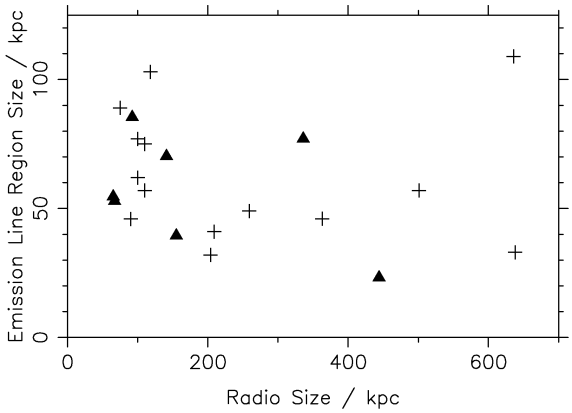

Figure 20. The variation of the linear extent of the [O II] 3727-Å emission-line region with the size of the radio source, once corrections for the lower S/N ratio of the 6C data have been included. 6C galaxies are marked as filled triangles, and the 3CR galaxies studied by Best et al. are marked as crosses.

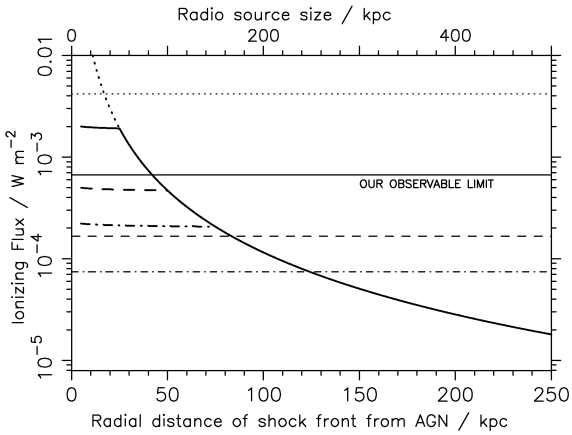

Figure 21. The changing contribution of ionizing photons from shocks and the AGN with radio size. Four clouds are considered, located at distances of 10, 25, 50 and 75 kpc from the AGN. Horizontal lines represent the constant flux received from the 5×10^{39} W AGN by each cloud. The contribution from the ionizing shock varies with time, and the changing flux received by each cloud is denoted by the four remaining lines. Dotted tracks model the flux received by the cloud at 10 kpc; solid tracks model the flux received by the cloud at 25 kpc; dashed tracks model the flux received by the cloud at 50 kpc; and dot-dashed tracks model the flux received by the cloud at 75 kpc. The horizontal solid line also represents the limiting flux of photons required by the clouds at a given radius in order for them to be observed at the sensitivity of our observations. For large radio sources, the observed maximum extent of apparently purely photoionized regions was ∼25 kpc; this line therefore coincides with the line representing the flux received by a cloud at 25 kpc from a typical AGN.

emission-line luminosities of 10^{35} to 10^{36} W (which constitutes the majority of the cooling), it is clear that these direct shocks are not the dominant source of ionization. Further proof of this is that the emission-line regions do not trace out the shock front, but seem to extend throughout the volume of the cocoon.

Although direct ionization of the cool clouds by shocks cannot adequately explain the observations, the hot phase has a filling factor of unity, and the properties of the emission-line regions may be better explained by the UV photon field produced by the cooling post-shock hot gas at the edges of an expanding radio source. Assuming that the hot gas obeys the scaling relations of Dopita & Sutherland (1996), entire shells of the hot-phase material can become radiative and act as a photon source for the cool phase. These photons travel both upstream and downstream from the shock, creating a precursor H II region upstream and strongly influencing the temperature and ionization state of the post-shock gas. Indeed, the location of the 6C galaxy data on the line ratio diagnostic diagram (Fig. 14) indicates that those shock models which include a precursor ionization region provide a better description of the ionization state for the small radio sources.

The UV luminosity of the hydrogen ionizing radiation field is given by Dopita & Sutherland (1996) as

$$L_{\rm UV} = 1.11 \times 10^{-6} \left(V_{\rm s} / 100\,{\rm km\,s^{-1}} \right)^{3.04} (n/10^6\,{\rm m^{-3}})\,{\rm W\,m^{-2}}\,.$$

The expanding radio cocoon can be approximated as an expanding sphere centred on the AGN. Before the shock front reaches a given cool, dense gas cloud, the flux of ionizing photons received from the shock as it passes through the hot, diffuse gas will be roughly the same as that of a point source with the same total luminosity as the shock. Beyond this point, the evolution (with increasing size of the radio source) of the flux of ionizing photons from the shock that reach the cloud then depends upon how the density of the external hot, diffuse gas decreases with distance from the host galaxy, and how the velocity of the bow shock varies with radio source size.

In a study of FRII galaxy environments, Wellman, Daly & Wan (1997) found that the variation of the density of the hot, diffuse gas surrounding radio galaxies could be well fitted by King profiles of the form

$$n(r) = n_0 \left[1 + (r/r_{\rm c})^2 \right]^{-3\beta/2},$$

with central density $n_0 \sim 3 \times 10^4$ m^{-3}, core radius $r_{\rm c} \sim 50$–75 kpc and $\beta \sim 0.7$. Studies of radio galaxies and clusters by Neumann (1999), Siebert, Kawai & Brinkmann (1999) and Heinz et al. (2002) have found similar values for these parameters. The density of the emission-line gas can therefore be approximated as roughly constant within the core radius (50 kpc) and decreasing proportional to r^{-2} significantly beyond this. Kaiser & Alexander (1997) predict that, in the self-similar expansion of the cocoons, if the environmental density can be approximated as a power law, $n \propto r^{-\gamma}$, then the radio source grows with time as: $D_{\rm rad} \propto t^{3/(5-\gamma)}$. For small radio sources ($\gamma = 0$), the expansion velocity of the radio source bow shock therefore depends on the source age and/or size as: $v \propto t^{-2/5} \propto D_{\rm rad}^{-2/3}$. At the other extreme, the expansion velocity of the largest radio sources in the sample will be approximately constant (since $\gamma \sim 2$). We have combined this variation in expansion velocity with radio source size with a King profile density model. Integrating over the total surface area of the shock front, the total output energy from the expanding shock front remains constant over time as it passes through the diffuse gas. The flux of UV photons received by a cool, dense gas cloud from this expanding shock front is roughly constant prior to the shock front reaching the cloud. Once the shock has passed through a cloud, the flux of photons received by the cloud decreases as $D_{\rm rad}^{-2}$ as the radio source grows.

Using the scaling relations of Dopita & Sutherland (1996) and a mean shock velocity at 12 kpc of $0.02c$ in the diffuse IGM surrounding the clouds, the precursor luminosity per unit area of the shock front varies with radio source size from over 10^{-3} W m^{-2} within 20 kpc from the AGN to $\sim 10^{-4}$ W m^{-2} at a distance of roughly 100 kpc. Our observations indicate that the extent to which we can observe a purely photoionized emission-line region is about 25 kpc from the host galaxy. A cloud at this distance would receive a flux density of $\approx 6.7 \times 10^{-4}$ Wm^{-2} from a typical point source of luminosity 5×10^{39} W (McCarthy 1993). This is approximately the same

as the flux density of a shock at about 40 kpc. For different values of the shock velocity, ambient gas density and AGN power, shocks can provide a greater or lesser flux of ionizing photons than the central engine. It is quite feasible that the precursor field produced by the shocks associated with the expansion of the radio source can ionize the emission-line regions out to distances of 50–60 kpc.

This model is illustrated in Fig. 21, which shows the changing contribution of ionizing photons to gas clouds at different distances from the AGN as the radio source expands. For all but the very smallest radio sizes, the ionization state of a cloud at 10 kpc is dominated by photoionization by the AGN. However, for radio sizes <10 kpc, our assumed values for V_s and n are not valid, as the presence of the host galaxy is not included in our model. The ionization state of a cloud at 25 kpc is dominated by the effect of shocks when the radio source is small (20 kpc $\lesssim D_{\rm rad} \lesssim$ 70 kpc). Emission from a cloud at 50 kpc from the AGN would be shock-dominated out to radio sizes of ∼150 kpc, but would only be observed in our data out to radio source sizes less than or comparable to the size of the EELR; the combined flux of ionizing photons from the shock and the AGN is approximately the same as that from the AGN at a distance of 25 kpc. The emission from such a cloud will be dominated by shock ionization. Clouds at a greater distance from the AGN than this will not be observable in this model at the sensitivity of our observations.

We note that the expanding shock front is not strictly spherical, as considered in this model, but propagates at different velocities at different locations on the cocoon. The shock will be most luminous near the radio source hotspots, by a factor of ∼30–60 for radio sources with $D_{\rm rad} < 120$ kpc. This will enhance the alignment effect. An alternative source of ionizing shocks is interactions between individual gas clouds and the radio jet. Although this would lead to shocked gas clouds closely aligned with the radio axis, the variation in EELR size with radio source size is much more difficult to explain.

An important question is whether or not such luminous shocks are permitted by UV and X-ray observations of radio galaxies. The total number of ionizing photons emitted from the radio source bow shocks is comparable to that of a luminous quasar; however, the spectral energy distribution of the shock waves is considerably steeper in the UV. The shock models of Dopita & Sutherland (1996) predict a flux density of 4×10^{-21} W m^{-2} Å^{-1} at a rest-frame wavelength of 1800 Å for the shock parameters considered above. The flux densities of 3CR sources at $z \sim 1$ are $\sim 5 \times 10^{-21}$ W m^{-2} Å^{-1} in the rest-frame waveband 1670–1890 Å as observed through a 1.5 arcsec slit (Best et al. 2000a). Since these observations include only a fraction of the shocked gas, the shock models cannot be excluded. Observations of higher redshift radio sources are also in agreement with this result; the predicted flux density of the shock models does not exceed the continuum flux density observed in the spectra of 6C radio sources at redshifts out to $z > 2$ (Jarvis et al. 2001).

The soft X-ray emission from the shock falls off rapidly with photon energy. For the parameters of our shock model, the shock front would have a flux density $\sim 10^{-7}$ W m^{-2} for $h\nu > 0.5$ keV. X-ray observations of 3C radio sources (e.g. Allen et al. 2001; Worrall et al. 2001) have found upper limits to the X-ray flux density of about 3–10 times greater than this value. The observations often show holes in the X-ray emission, coincident with the lobes of the radio source. These cavities are surrounded by bright X-ray emission, which can be modelled as limb-brightened shells of gas formed by the displacement and compression of material by the expansion of the radio source. The brightest X-ray emission from 3C 317 (Blanton et al. 2001) is coincident with the Hα + [N II] contours of Baum et al. (1988), providing evidence for cooler gas in these regions as well. Note that it is the hot intercloud gas that emits at X-rays, rather than the cooler gas clouds. If the cool clouds were heated to temperatures $T \geqslant 10^6$ K, the gas would not be able to cool by line emission and no line emission would be observed, regardless of whether the gas was ionized by shocks or the AGN.

In general, then, this model fits the observational data very well. For the very smallest radio sources, it is expected that the flux of ionizing photons from the AGN is of far greater importance than those produced by any ionizing shocks associated with the expanding radio cocoon. Jarvis et al. (2001) observe no shock boosting of the Lyman alpha line in small radio sources, and Hirst, Jackson & Rawlings (2002) provide tentative evidence that [O III] is not boosted in compact steep spectrum (CSS) sources, consistent with this model. The observed reduction in Balmer line flux of the small radio sources confirms the presence of ionizing shocks in these sources (Morse et al. 1996), rather than indicating a reduction in ionizing photons. Further, Moy & Rocca-Volmerange (2002) have considered the predictions of combined shock ionization and photoionization models. Comparing the emission-line ratios of a large number of radio galaxies and quasars, they also find that both ionization processes are likely to be occurring in the emission-line regions of galaxies with radio sizes 2 kpc $< D_{\rm rad} <$ 150 kpc, with pure photoionization by the AGN remaining the best interpretation for the emission-line regions of the smallest and largest sources.

An interesting aspect of this model is that, if a cloud at 50 kpc radius can be ionized by shocks as they approach this radius, that cloud should, in principle, also be ionized by shocks when the radio source has much smaller radius. In practice, however, the line emission is generally not seen much beyond the limit of the radio emission. At first sight this seems to argue against such strong shock contributions. However, even in the smallest sources there is no observable emission from much beyond the radio source, in regions where photoionization should be occurring. This suggests that the lack of line emission from these regions is not necessarily a problem with the shock models; rather, a general feature of radio sources is that the emission-line regions become much more luminous after the passage of the radio sources. Further evidence in support of this comes from observations that the emission-line regions around radio-quiet quasars are not significantly extended (Telfer, Kriss & Tsvetanov 2000) whilst those of radio-loud quasars show extensions comparable to those of radio galaxies (Crawford & Vanderriest 2000).

Clearly, regardless of the ionizing photons that it supplies, the expanding radio source somehow directly increases the emission-line observability of regions through which it has passed. One possibility is that the gas clouds in the EELR are dragged out from a more central region of the galaxy by the radio source for a limited distance and/or time, and so are only present at these large radii after the passage of the radio source. However, our modelling shows that clouds at distances of >25 kpc from the AGN *can* be in place prior to the expansion of the radio source and yet not be observed, and that clouds at a distance greater than 60 kpc from the AGN cannot be ruled out. The presence of extended Lyman-α haloes around radio galaxies (e.g. van Ojik et al. 1997) provides further evidence that dense gas clouds may exist out to large radii around radio sources of all sizes. An alternative possibility is that the passage of the radio jet disrupts large, optically thick emission-line clouds, producing smaller optically thin clouds which increases the covering factor for absorption of AGN radiation (cf. Bremer, Fabian & Crawford

1997). This appealing possibility also helps to explain the radio size evolution of the optical alignment effect.

5.3 Emission-line region kinematics

The velocity FWHM of the emission-line gas is strongly anticorrelated with radio size for both 6C and 3CR galaxies. This is interpreted as the boosting of the observed FWHM of small sources by shock acceleration and entrainment of the emission-line gas clouds over that observed in the larger photoionized sources. The correlation of both the kinematic and ionization properties of the radio galaxies with radio size within both samples indicates that these are related, regardless of the difference in radio power between the 3CR and 6C galaxies. For the 6C sources, the range of velocities observed displays a weaker correlation with emission-line region size and FWHM than the more powerful 3CR sources.

One difference between the two samples is the range of velocities observed in the sources, which appears to decrease with both radio power and radio size. The weaker 6C radio sources display a somewhat lesser degree of variation in the emission-line gas kinematics than is seen among the 3CR galaxies. This is not likely to be caused by any effects of the lower S/N of the 6C observations; no evidence is seen in Figs 1–10 that the fitting procedures are missing further velocity components at greater spatial extents than the regions currently analysed. If confirmed by a larger data set, the variation in velocity range with radio power could have several different explanations.

Large radio sources at $z \sim 1$ have velocity profiles consistent with rotation (Best et al. 2000b), as do 3CR sources at low redshifts (Baum, Heckman & van Breugel 1992). *K*-band observations show that $z \sim 1$ 6C radio galaxies are fainter by $\sim$0.6 mag (Eales et al. 1997; Inskip et al. 2002) than 3CR galaxies at the same redshift. If this is due to a difference in host galaxy mass, the rotation profiles of the less massive 6C galaxies would be a factor of $\sim$1.3 less. The velocity profiles could alternatively indicate infall or outflow of material. For small radio sources, the extreme gas kinematics observed may be due to shocks associated with the radio jet and/or the expansion of the radio source, and would therefore be strongly correlated with radio jet kinetic power, and hence the luminosity of the radio source. The mean velocity range of small 3CR galaxies is 45 per cent greater than that observed for small 6C galaxies, although this result is based on a very small number of sources. The more extreme kinematics of the 3CR sources are as expected, given their greater radio power.

6 CONCLUSIONS

Very deep spectroscopic observations have been made of an unbiased subsample of eight 6C galaxies at $z \sim 1$. Many emission lines have been observed over the rest-frame wavelength range 1500–4500 Å, and a study of the 2D kinematics of the emission-line gas has been carried out. Our conclusions can be summarized as follows:

(i) The observed spectra of the 6C galaxies are quite varied, both in the strength of the emission lines observed, and in the line ratios observed.

(ii) The composite spectra of the 6C galaxies are similar to those of Best et al. (2000a) for the 3CR sources at the same redshift.

(iii) 6C sources with $D_{\rm rad} > 120$ kpc host less powerful AGN than 3CR sources of a similar size at the same redshift. Their spectra are well explained by photoionization, typically with a lower ionization parameter than their more powerful 3CR counterparts. The total emission-line luminosities of large 6C sources are also smaller than that of large 3CR sources, and their emission-line regions are observable out to smaller physical scales.

(iv) For small radio sources, $D_{\rm rad} < 120$ kpc, a combination of AGN photoionization and shock ionization provides the best explanation of their spectra. Their emission-line regions typically have a similar size to the extent of the radio source.

(v) The velocity profiles of shock-ionized EELRs are distorted, whereas photoionized EELRs display smooth velocity profiles.

(vi) The ionization properties of the subsample can be explained by a simple model incorporating photoionization by the AGN and a luminous shock associated with the expanding radio source.

(vii) The kinematics of the EELRs of 6C radio sources are similar to those of more powerful 3CR sources.

(viii) A high-velocity component is observed in the EELR of 6C 1019+39 at $\sim$700 km s^{-1}, close to the host galaxy.

In summary, the properties of 6C radio galaxies at $z \sim 1$ are similar to 3CR sources at the same redshift, despite the decrease in radio power between the samples. A strong anticorrelation of emission-line luminosity with source size is found. In addition, we also find tentative evidence that the range of velocities observed in the emission-line gas is most likely dependent on the properties of the radio source rather than the underlying gravitational potential of the host galaxy. In a companion paper (Paper II), this data set is compared with lower redshift sources of the same radio power to break the radio power -redshift degeneracy, and to investigate the intrinsic dependences of radio galaxy properties on redshift, radio power and source age.

ACKNOWLEDGMENTS

This work was supported in part by the Formation and Evolution of Galaxies network set up by the European Commission under contract ERB FMRX-CT96-086 of its TMR programme. KJI acknowledges the support of a PPARC research studentship. The William Herschel Telescope is operated on the island of La Palma by the Isaac Newton Group in the Spanish Observatorio del Roque de los Muchachos of the Instituto de Astrofísica de Canarias. This research has made use of the NASA/IPAC Extragalactic Database (NED) which is operated by the Jet Propulsion Laboratory, California Institute of Technology, under contract with the National Aeronautics and Space Administration. PNB is grateful for the generous support offered by a Royal Society Research Fellowship. We would like to thank the referee for useful comments.

REFERENCES

Allen M. G., Dopita M. A., Tsvetanov Z. I., 1998, ApJ, 493, 571
Allen S. W. et al., 2001, MNRAS, 324, 842
Baldwin J. E., 1982, in Heeschen D. S., Wade C. M., eds, Extragalactic Radio Sources, Proc. Symp. No. 97. Reidel, Dordrecht, p. 21
Baum S. A., Heckman T. M., 1989, ApJ, 336, 702
Baum S. A., McCarthy P. J., 2000, ApJ, 119, 2634
Baum S. A., Heckman T. M., Bridle A., van Breugel W. J. M., Miley G., 1988, ApJS, 68, 643
Baum S. A., Heckman T. M., van Breugel W. J. M., 1992, ApJ, 389, 208
Best P. N., Longair M. S., Röttgering H. J. A., 1997, MNRAS, 292, 758
Best P. N., Eales S. A., Longair M. S., Rawlings S., Röttgering H. J. A., 1999, MNRAS, 303, 616
Best P. N., Röttgering H. J. A., Longair M. S., 2000a, MNRAS, 311, 1
Best P. N., Röttgering H. J. A., Longair M. S., 2000b, MNRAS, 311, 23
Binette L., Wilson A. S., Storchi-Bergmann T., 1996, A&A, 312, 365

Blanton E. L., Sarazin C. L., McNamara B. R., Wise M. W., 2001, ApJ, 558, L15
Boyle B. J., 1990, MNRAS, 243, 231
Bremer M. N., Fabian A. C., Crawford C. S., 1997, MNRAS, 284, 213
Carter D. et al., 1994, The Isis Double Beam Spectrograph v1.0. WHT, Isaac Newton Group of Telescopes, La Palma. http://www.ing.iac.es/Astronomy/observing/manuals/html_manuals/wht_instr/isis_hyper/isis_hyper.html
Crawford C. S., Vanderriest C., 2000, MNRAS, 315, 433
de Breuck C., Röttgering H., Miley G., van Breugel W., Best P., 2000, A&A, 362, 519
Dey A., van Breugel W., Vacca W. D., Antonucci R., 1997, ApJ, 490, 698
di Serego Alighieri S., Cimatti A., Fosbury R. A. E., 1994, ApJ, 431, 123
Dopita M. A., Sutherland R. S., 1996, ApJS, 102, 161
Eales S. A., 1985, MNRAS, 217, 149
Eales S. A., Rawlings S., Law-Green D., Cotter G., Lacy M., 1997, MNRAS, 291, 593
Evans I., Koratkar A., Allen M., Dopita M., Tsvetanov Z., 1999, ApJ, 521, 531
Francis P., Hewett P., Foltz C., Chaffee F., Weyman R., Morris S., 1991, ApJ, 373, 465
Heinz S., Choi Y. Y., Reynolds C. S., Begelman M. C., 2002, ApJ, 569, 79
Hirst P., Jackson N., Rawlings S., 2002, MNRAS, submitted
Howarth I. D., 1983, MNRAS, 203, 301
Inskip K. J., Best P. N., Longair M. S., MacKay D. J. C., 2002, MNRAS, 329, 277
Jarvis M. J. et al., 2001, MNRAS, 326, 1563
Kaiser C. R., Alexander P., 1997, MNRAS, 286, 215
Kaiser C. R., Dennett-Thorpe J., Alexander P., 1997, MNRAS, 292, 723
McCarthy P. J., 1993, ARA&A, 31, 639
McCarthy P. J., Spinrad H., van Breugel W., 1995, ApJSS, 99, 27
Mendoza S., 2000, PhD thesis, Cambridge Univ.
Morse J. A., Raymond J. C., Wilson A. S., 1996, PASP, 108, 426
Moy E., Rocca-Volmerange B., 2002, A&A, 383, 46
Neumann D. M., 1999, ApJ, 520, 87
Osterbrock D. E., 1989, Astrophysics of Gaseous Nebulae and Active Galactic Nuclei. University Science Books, Mill Valley, CA
Osterbrock D. E., Martel A., 1992, PASP, 104, 76
Rawlings S., Saunders R., 1991, Nat, 349, 138
Rawlings S., Eales S., Lacy M., 2001, MNRAS, 322, 523
Scheuer P. A. G., 1974, MNRAS, 166, 513
Siebert J., Kawai N., Brinkmann W., 1999, A&A, 350, 25
Solórzano-Iñarrea C., Tadhunter C. N., Axon D. J., 2001, MNRAS, 323, 965
Stern D., Dey A., Spinrad H., Maxfield L., Dickinson M., Schlegel D., González R. B., 1999, AJ, 117, 1122
Sutherland R. S., Bicknell G. V., Dopita M. A., 1993, ApJ, 414, 510
Tadhunter C. N., 1991, MNRAS, 251, 46P
Telfer R. C., Kriss G. A., Tsvetanov Z., 2000, AJ, 120, 2363
van Ojik R., Röttgering H. J. A., Miley G. K., Hunstead R. W., 1997, A&A, 317, 358
Wellman G. F., Daly R. A., Wan L., 1997, ApJ, 480, 96
Willott C. J., Rawlings S., Blundell K. M., Lacy M., 1999, MNRAS, 309, 1017
Worrall D. M., Birkinshaw M., Hardcastle M. J., Lawrence C. R., 2001, MNRAS, 326, 1127

APPENDIX A: FAINT BROAD COMPONENTS IN THE [O II] 3727-Å LINE OF 6C AND 3CR GALAXIES

In light of the results of Solórzano-Iñarrea et al. (2001), as described in the Introduction, we have undertaken a search for such underlying broad components in the [O II] 3727-Å lines of the 6C subsample, and also in the spectroscopic data for the 3CR subsample of Best et al. (2000a,b). In the main body of the paper, previous fitting of a 2D region around the [O II] emission line used a series of extracted spectra four pixels in width, stepped every two pixels, with the purpose of investigating the spatial variations of the emission-line properties. As already noted in Section 3.1, a single Gaussian fit to the emission-line data was inadequate in several cases. The peak flux was often underestimated for these sources, coupled with a poor fit at high velocities, as expected for misfitting the combination of a narrow line with a faint broad component. An alternative explanation is that the line profiles may be non-Gaussian.

We have used a similar process for fitting weak broad components to the emission line using a single wider spectrum extracted from the centre of each source, thus increasing the signal-to-noise ratio over that of the previous extracted spectra. The new extracted region was typically nine pixels (3.24 arcsec) in spatial extent. A wider extracted region could have been used, but in such a situation any velocity gradient present in the 2D spectrum would mimic an underlying broad component in the data. The same constraints were used as for narrow-line fitting, with the additional restrictions that any broad component should be fainter and have a wider FWHM than the first Gaussian fitted to the data.

Of the 22 6C and 3CR sources studied, only six showed clear evidence for an underlying broad component, with a single Gaussian (or two Gaussians for the sources with more than one distinct component) providing a larger reduced χ^2 than that achieved with the addition of another Gaussian component. These were 3C 22, 3C 217, 3C 247, 3C 265, 3C 280 and 3C 441. Several other sources were also poorly explained by a single Gaussian fit; however, in these cases additional components gave no improvement in the reduced χ^2. The two-Gaussian reduced χ^2 for 6C 1017+37 was comparable to that for a single Gaussian; for this source the presence of an additional component is uncertain. The fact that six 3CR sources showed evidence for broad components whilst none of the 6C sources did is not necessarily significant since the presence of an underlying broad

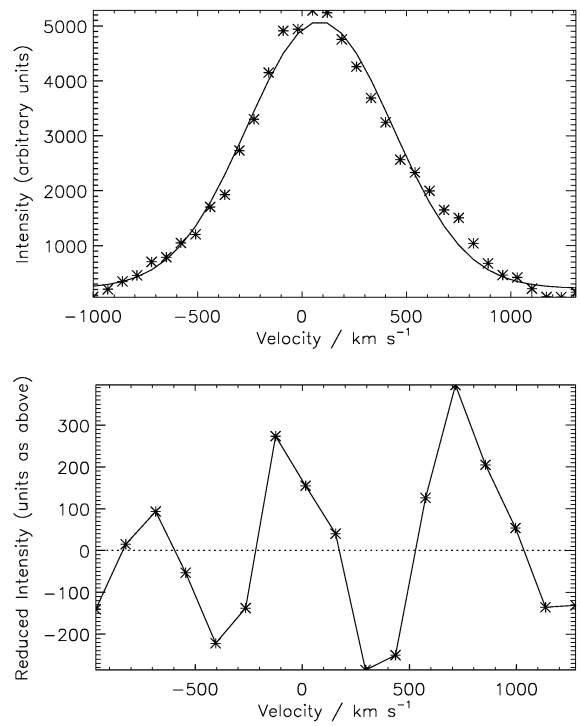

Figure A1. Searching for underlying broad components in the [O II] 3727-Å emission line. (a) Single-Gaussian fit to the extracted line flux for six sources showing evidence for an underlying broad component. (b) Residuals of the single-Gaussian fit.

component was rejected for sources for which the two-Gaussian reduced χ^2 was less than that for the single-Gaussian fit and the lower signal-to-noise ratio of the 6C data is an important detriment to improving the fit.

We found that, in the instances for which a broad component is required, several different combinations of two or more Gaussians had comparable reduced χ^2. As well as the expected bright narrow line with a weak underlying broad component, the data were also generally well fitted by a somewhat fainter narrow Gaussian coupled with a strong, broad component. The fairly low S/N of the data allowed many possible groups of Gaussians to fit the data well within experimental error, and so we are unable to determine exactly the parameters of any actual underlying broad component in the emission lines of the sources studied. We can, however, gain a greater understanding of the inadequacies of single-Gaussian fitting, which generally underestimates the peak of the line, and misfits the shape of the wings. We combined the emission-line data of the six sources showing evidence for some underlying broad component, by centring their peaks and re-binning the data to the same FWHM. A single Gaussian was fitted to the resulting combination; this and the residuals obtained are plotted in Fig. A1. This clearly shows how a single Gaussian misfits the data.

On the whole, the necessity for broad components is seen to be more likely in intermediate to small radio sources. This is certainly in agreement with the shock-related origins of broad components, as larger sources are in general seen to be photoionized. On the other hand, the very smallest sources do not exhibit clear evidence for broad components in their emission lines. However, the complex shock-induced velocity structures of these sources, already fitted by multiple Gaussians, will inhibit the fitting of further velocity components. Thus, whilst broad components may indeed be present in these heavily shocked smaller sources, they cannot be conclusively identified from these data. The work of Solórzano-Iñarrea et al. (2001) benefited from a higher S/N than our data, as their observations were made with a much lower spectral resolution.

This paper has been typeset from a TEX/LATEX file prepared by the author.